7-1-2004

Going Slitless: Images of Forbidden Line Emission Regions of Classical T Tauri Stars Observed with the Hubble Space Telescope

Patrick Hartigan
Rice University

Suzan Edwards
Smith College, sedwards@smith.edu

Rachel Pierson
Rice University

The Astrophysical Journal, 609:261–276, 2004 July 1

GOING SLITLESS: IMAGES OF FORBIDDEN-LINE EMISSION REGIONS OF CLASSICAL T TAURI STARS OBSERVED WITH THE *HUBBLE SPACE TELESCOPE*[1]

Patrick Hartigan,[2] Suzan Edwards,[3] and Rachel Pierson[2]
Received 2003 August 7; accepted 2004 March 9

ABSTRACT

We have observed five classical T Tauri stars known to have strong forbidden-line emission with STIS in slitless mode on the *Hubble Space Telescope*. This technique makes it possible to image jets within a few tens of AU of their exciting sources, a region of great interest for models of accretion disks and jets. Slitless images generate emission-line images at all wavelengths, including those where no narrowband filters exist. Images of the forbidden-line regions around each object, constructed by subtracting the stellar continuum and combining observations taken at different orientations, show [O I] jets from CW Tau, HN Tau, UZ Tau E, DF Tau, and the primary of DD Tau. Jets exist on both sides of the close binary DF Tau, either as a jet and its counterjet or as separate jets from the primary and secondary. Several emission lines not previously seen in jets close to the star exist in the HN Tau jet; the [Fe II] $\lambda7155/\lambda8617$ ratio is particularly useful because it measures the electron density in the densest regions of stellar jets, where $\log N_e \gtrsim 6$. Electron densities in the inner 30 AU of the HN Tau jet range from $\log N_e = 6.2$ to 6.9. We construct diagnostic diagrams for the density, temperature, and ionization fraction in jets close to their stars, using various emission lines of O I and O II. The red auroral [O II] lines are bright close to HN Tau, indicating that the emitting regions of the inner 35 AU of the jet have a substantial ionized component—20% if the emission comes from a shock and 50% for an isothermal flow. We discuss mass-loss rates and filling factors for these two cases. The intensity of the HN Tau jet in [O I] $\lambda6300$ declines exponentially with distance beyond $\sim$15 AU. The superior continuum subtraction with slitless data, as compared with narrowband images, makes it possible to resolve the widths of jets at distances as close as $\sim$15 AU from the star. The two best examples, HN Tau and UZ Tau E, have jets that expand with distance. When projected back to the source, the width of the jet in HN Tau is a few AU at the 3 σ level, while the jet in UZ Tau E is spatially unresolved. The new images of CW Tau reveal proper motions in this jet, which has ejected at least two knots since 1980. There is no indication that CW Tau brightened when it ejected the largest of these knots, but the photometric record of this star over the last two decades is fragmentary.

Subject headings: circumstellar matter — stars: pre–main-sequence

1. INTRODUCTION

Accretion disks and collimated outflows govern many of the observational characteristics of young stars and play a crucial role in the star formation process. Surveys of star-forming regions have found that the majority of young stars are surrounded by an accretion disk that radiates in the infrared as material moves through the disk toward the star (Hillenbrand et al. 1998; Haisch et al. 2001) and in the ultraviolet and optical as material impacts the stellar photosphere (Gómez de Castro & Fernández 1996; Hartigan et al. 1991). Permitted emission lines in T Tauri stars typically have redshifted absorption features that form as disk material falls onto the star and sometimes also show blueshifted absorption, indicating outflow (Edwards et al. 1994). Outflows from low-mass stars, which emerge along the rotation axis of the disk (e.g., Burrows et al. 1996), manifest themselves as highly collimated, supersonic stellar jets that can extend for parsecs (Devine et al. 1997) and as less collimated, slower, bipolar molecular outflows (Richer et al. 2000). Stellar jets often appear as a series of bow shocks driven by velocity variations in the flow (Reipurth & Bally 2001).

Outflows affect the process of star formation in several ways. As in the present solar system, most of the angular momentum in accretion disks resides in the disk and not in the central object. Jets provide a means to remove the angular momentum brought in by accreting material in the disk, and some evidence now exists that jets rotate (Bacciotti et al. 2002). Models of self-similar MHD winds from accretion disks (Ferreira 1997; Casse & Ferreira 2000) predict the mass outflow rate to be a sizable fraction (1%–10%) of the mass accretion rate (see also Shu et al. 2000; Königl & Pudritz 2000), and there is observational evidence to support this connection (Cabrit et al. 1990; Hartigan et al. 1995, hereafter HEG95). At larger scales, outflows collide with and heat molecular clouds, which helps to energize the clouds against further collapse. Cavities created by outflows create a fractal-like structure within the cloud and expose protoplanetary disks to ambient ultraviolet radiation.

Surveys show that most pre–main-sequence stars are binaries (Ghez et al. 1993; Leinert et al. 1993), although we are just beginning to understand how companions affect accretion and outflow. When binaries are separated widely compared to the size of their disks, accretion and outflow probably operate in much the same way as they do in single stars. However, when the orbital semimajor axis is $\lesssim$100 AU (0.″7 at 140 pc),

[1] Based on observations made with the NASA/ESA *Hubble Space Telescope* (*HST*), obtained at the Space Telescope Science Institute (STScI), which is operated by the Association of Universities for Research in Astronomy (AURA), Inc., under NASA contract NAS5-26555.

[2] Department of Physics and Astronomy, Rice University, 6100 South Main, Houston, TX 77005-1892.

[3] Five College Astronomy Department, Smith College, Northampton, MA 01063.

a substantial circumbinary disk should form around the system (e.g., Close et al. 1998). The stars still retain their circumstellar disks, with both primary and secondary typically showing accretion activity (White & Ghez 2001). However, accretion rates are highly correlated in subarcsecond binaries, so the systems are no longer independent (Hartigan & Kenyon 2003). Little is known about accretion properties of spectroscopic binaries, but orbital mechanics dictates that the stars share a large circumbinary disk, which feeds material onto the stars directly or onto circumstellar disks a few stellar radii in extent (Artymowicz & Lubow 1996).

Many T Tauri stars emit forbidden-line radiation, and because this emission is optically thin and line ratios constrain the temperature and electron density, it is an excellent way to study outflows. Forbidden-line emission from young stars tends to be blueshifted, as circumstellar disks obscure any redshifted emission. Typically dominated by the high critical density line [O I] λ6300, forbidden-line emission comes from a high-density, low-ionization flow (Edwards et al. 1987). Forbidden lines have distinct low- and high-velocity components. The low-velocity component lies within a few tens of AU of the star, is blueshifted by only a few km s^{-1}, and appears strongest in lines with high critical densities. In contrast, the high-velocity component is more extended spatially, has velocities of hundreds of km s^{-1}, and shows a lower density, like that of a stellar jet (HEG95; Hirth et al. 1997). The low-velocity component has been modeled as a disk wind, with the high-velocity component in a jet (Kwan & Tademaru 1995). Recent ground-based and *HST* observations of forbidden lines show that the high-velocity material is more confined along the axis of the flow (Lavalley et al. 1997; Bacciotti et al. 2000), consistent with the above scenario.

To make progress in connecting accretion with outflow, we need to study jets as close as possible to their driving sources. The main observational goals are to detect as many emission lines as possible and to use these to diagnose physical conditions, such as density, temperature, ionization fraction, and collimation, throughout the jet. Following proper motions in jets also provides a link between outflow and accretion and makes it possible to measure the inclination of the system and learn about fluid dynamics in the jet. In binaries, we would like to know if both stars drive jets and, if so, whether or not the jets (and by inference the rotation axes of the disks) are aligned.

In observational terms the above goals translate into obtaining images of many emission lines with the best spatial resolution possible of jets that emerge from bright stars. In this paper we explore slitless spectroscopy with *HST* as a technique for imaging stellar jets. Slitless spectra are images of every object in the field at all wavelengths; hence, all emission lines can be imaged, including those that lack narrowband filters. For example, in our data the *y*-axis is a spatial direction in the raw images, and the *x*-axis is the other spatial direction and also the dispersion direction.

Slitless spectra work well for imaging stellar jets because extinction from surrounding dark clouds makes star fields near most T Tauri stars sparse at optical wavelengths. Hence, overlapping spectra are not a problem, except for close binaries or for the jet itself, whose image lands on top of the stellar spectrum if the dispersion direction is parallel to the jet. For this reason, with slitless data it is important to observe T Tauri stars at different orientations relative to the dispersion direction if the axis of the jet is not known a priori. At the low spectral resolution of the observations in this paper, radial velocities are small and generate negligible shifts in the images, but line blending is an issue for pairs of lines that are within $\sim$20 Å of each other. Possibly the biggest drawback is that the technique is relatively uncommon, so calibrations and data reduction can be challenging.

For T Tauri jet work with *HST*, slitless imaging is an especially powerful technique for measuring widths of jets very close to the source, where accurate continuum subtraction is essential. The spatial extent of the stellar spectrum gives an observational measure of the point-spread function (PSF) taken at the same time as the image, and in principle it is straightforward to subtract continuum from the images. Slitless images are also an excellent way to follow velocity-averaged emission-line ratios as a function of distance.

Each of the objects in this study brings something new to bear on the subject of disks and jets. All are members of the nearby Taurus-Auriga star formation region ($d \sim 140$ pc), so the objects are relatively bright and are easier to resolve at scales of a few tens of AU than are more distant objects like those in Orion. When combined with previous images of the well-studied jet in CW Tau, the new slitless images reveal proper motions in the jet for the first time and thereby clarify the geometry of the flow. The proper motions enable an important test of the accretion-outflow connection, which predicts a rise in brightness of the central source when the knot formed; the knot is close enough to the star, and therefore young enough, that this event occurred in the era of modern photoelectric photometry. DD Tau, DF Tau, and UZ Tau E are subarcsecond binaries and give the first glimpse as to how flows operate in pairs where the separation between the stars is smaller than a typical disk size. Finally, the multiple lines imaged by the slitless method in the extended jet of HN Tau open up new emission-line diagnostics that are essential for studying the dense environments in jets close to the star. The slitless data also provide the best information to date on the opening angles of stellar jets and the physical size of their source regions.

2. OBSERVATIONS AND DATA ANALYSIS

We obtained slitless images of five classical T Tauri stars that have strong forbidden-line emission, CW Tau, DD Tau, DF Tau, HN Tau, and UZ Tau E, using the CCD detector and G750L grating in the Space Telescope Imaging Spectrograph (STIS) on the *HST* between 1999 September 21 and 2000 December 13. Each target was observed at two position angles (P.A.s), separated by as close to 90° as scheduling constraints allowed. Two P.A.s are required to remove the stellar spectrum for extended flows that emerge at unknown P.A.s from the star. For example, the image of a jet that emerges from the star along the dispersion direction will lie on top of the stellar spectrum and will be indistinguishable from a broad stellar emission line; however, the same jet observed with the spacecraft rotated by 90° extends perpendicular to the stellar spectrum, so the image of the jet separates cleanly from the stellar spectrum.

Each P.A. for each target was observed for one *HST* orbit, with the total exposure time of $\sim$40 minutes. The final images combine two exposures, each of $\sim$20 minutes and CR-split, taken at two dither positions separated by $\sim$0.″2. The dithers were offset by an integral number of STIS pixels to minimize any interpolation errors. The two images for each object are easy to align using the bright emission lines present in the spectra. The scale on the images is 0.″05072 pixel^{-1}, which gives a field of view of about 52″, and the dispersion with the G750L grating is 4.882 Å pixel^{-1}.

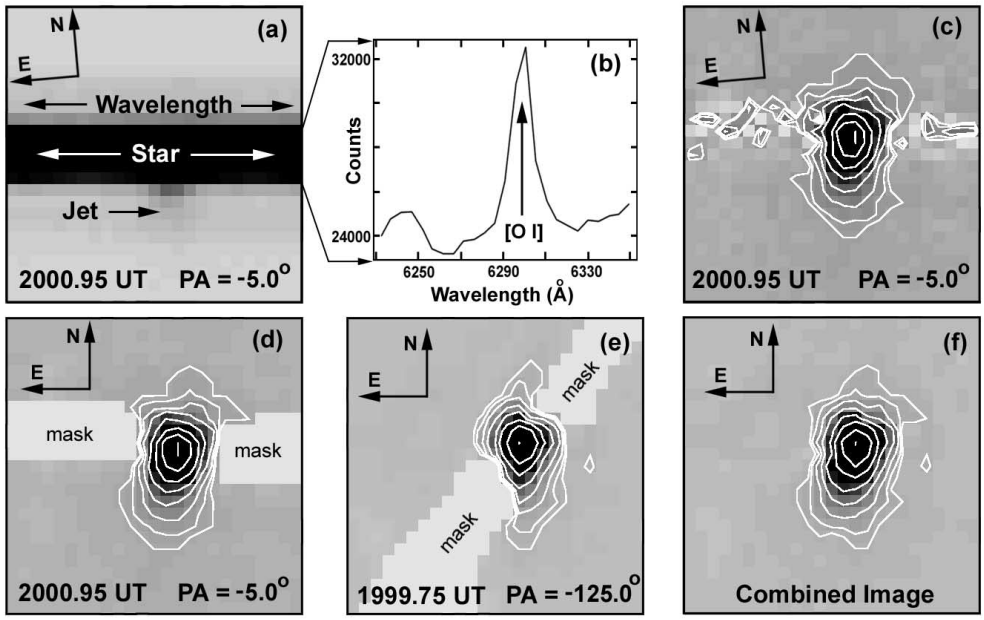

FIG. 1.—Extraction method for slitless images. The jet extends just below the stellar spectrum in (*a*), and the [O I] λ6300 line is easy to see in the extracted spectrum (*b*). The jet clearly extends to the south-southeast of the star when the stellar continuum is subtracted (*c*). Residuals from the subtraction are masked in (*d*), which is now rotated so north is up and east to the left. Combining this image with a similar one derived from a different P.A. (*e*) yields the final, combined image (*f*). Adjacent contour levels are separated by factors of 2. The lowest contour corresponds to 3.2×10^{-17} ergs cm^{-2} s^{-1} pixel^{-1}.

Image reductions followed the procedure described by Hartigan & Kenyon (2003) to remove hot pixels from the dark-subtracted, flat-fielded data. The cleaned images were corrected for fringing using flats taken for this purpose. Fringing corrections were negligible for wavelengths $\lesssim$8000 Å and were $\lesssim$10% for all the emission lines studied in this paper.

The *x*-axis is both a spatial direction and the direction of dispersion in our slitless data; hence, the location of a particular wavelength on the CCD depends on where it is in the field of view. For this reason, wavelength calibrations are not useful for these data. In practice, the Hα line is easy to see in all the stars, and a constant dispersion of 4.882 Å pixel^{-1} identifies all of the emission lines in the spectra to within a pixel. Slitless data have no aperture correction term, so the ratio of energy fluxes between emission lines equals the ratio of the counts, weighted by the energies of the transitions and the throughput of the system. Absolute calibrations also take into account the absolute sensitivity of the system, found from the calibration table associated with the spectra, the gain of the CCD, which was 4, the area of the *HST* mirror, and the exposure time. The absolute calibration of STIS is uncertain to $\sim$10%.

The main advantage of slitless spectroscopy over conventional narrowband imaging is the ability to completely remove the continuum, even when the continuum dominates the total flux. The concept of continuum removal is fairly straightforward and has been used in several ground-based emission-line studies of young stars (e.g., Solf 1987; Hirth et al. 1997; Pyo et al. 2002), although the present data require a somewhat more involved procedure than has been used in previous studies. The stellar PSF is easy to measure in the *y*-direction on either side of the line of interest. A linear interpolation of the continuum across the emission line removed most of the continuum, but frequently left spurious features associated with photospheric lines in the star. To improve the process, we extracted a stellar spectrum from the five rows where the star is brightest, at all wavelengths on either side of the emission line. Multiplying this spectrum by the stellar PSF along the *y*-axis, determined from a range of columns on either side of the line where no emission lines were present, produced a good stellar subtraction.

Essentially, this process uses the observed stellar spectrum and PSF to remove the star. What remains is any emission at the line of interest, plus any emission near this line that is distributed differently in the *y*-direction from a stellar component. In slitless images, jets may emerge at any angle from the rest wavelength of the line at the stellar position, depending on the P.A. of the telescope. Hence, it is important to be able to distinguish faint jet emission from the dominant stellar component everywhere in the vicinity of the line.

Figure 1 illustrates the procedure as applied to HN Tau, which has a bright jet that emanates from the star at a P.A. of $\sim$171°. The jet is barely visible in the first panel, although a spectral extraction across the brightest rows clearly shows the [O I] emission line, as well as photospheric features in the spectrum. The line clearly extends to the south-southeast when the continuum is removed. The image, rotated to make north up and east to the left and masked to remove residuals of the stellar spectrum, combines with a second image taken with the telescope oriented at a different P.A. to produce the final image. The final image sometimes benefits from deconvolution, which we did by using the Tiny Tim algorithm to generate a PSF at the wavelength in question and then applying the

TABLE 1
Position Angles and Separations

Name	P.A.[a] (deg)	Sep.[b] (mas)	UT Date
CZ Tau[c]	11.56 (0.05)	29992 (14)	1999.77
CZ Tau	89.0 (1.3)	328 (14)	1999.77
DD Tau	182.1 (1.0)	566 (14)	1999.77
	184.2 (1.0)	594 (14)	2000.78
DF Tau	272.3 (6.1)	100 (14)	1999.72
	268.0 (6.1)	112 (14)	2000.92
HN Tau	219.44 (0.1)	3132 (14)	1999.75
	219.57 (0.1)	3156 (14)	2000.95
UZ Tau W	3.4 (1.6)	369 (14)	1999.74
	4.1 (1.6)	367 (14)	2000.93
UZ Tau E[d]	93.25 (0.2)	3557 (14)	1999.74
	93.26 (0.2)	3549 (14)	2000.93

Note.—As determined from the STIS acquisition images.
[a] Position angle of the secondary relative to the primary (and errors).
[b] Separations (and errors).
[c] Separation of CZ Tau primary from DD Tau primary.
[d] Separation between UZ Tau W primary and UZ Tau E.

Lucy-Richardson algorithm in the STSDAS package of IRAF with eight iterations.

HST observations of the P.A.s and separations within binaries provide important data points that constrain the orbits, and ultimately the masses, of the primaries and secondaries. Two of the objects in this study, DF Tau and DD Tau, are subarcsecond binaries, while UZ Tau E and HN Tau have companions several arcseconds away. Another binary, CZ Tau, appears at the edge of the field in the 1999 image of DD Tau. Table 1 lists the astrometric information for all the binaries in our data set, measured from the unfiltered CCD acquisition images (see Hartigan & Kenyon 2003 for more details). Uncertainties in the P.A. and separation are dominated by errors in measuring the stellar positions, typically 0.1–0.2 pixels; uncertainties in the plate scale of STIS and orientation of *HST* are negligible in comparison.

3. RESULTS

3.1. [O I] *Images of Jets*

The individual, combined, and deconvolved [O I] λ6300 images of our five targets appear in Figures 2 and 3 and the equivalent widths and line fluxes in Table 2. The objects all have strong forbidden-line emission from ground-based spectra, and each has a resolved jet in the *HST* images. Our slitless data make it possible to obtain images of all of the emission lines; this capability is particularly important for HN Tau, which has numerous lines extended in the jet. The red [S II] doublet is blended when observed with the G750L grating and so is unsuitable for making images. Fortunately, the brightest forbidden line close to the stars is typically [O I] λ6300, which is uncontaminated by other lines. The two epochs, separated by about a year in all cases, allow us to address how each system varies spectroscopically. The three close binaries in our sample, DD Tau, DF Tau, and UZ Tau E, allow us to investigate how jets behave in binaries when the separations are smaller than the typical size of a circumstellar disk. We discuss each target below.

3.1.1. *CW Tau*

If there is a prototype for forbidden-line emission in T Tauri stars, it is probably CW Tau. The lines are bright and show distinct high- and low-velocity components (Edwards et al. 1987; HEG95). A jet emerges from the star toward the southeast at a P.A. of about 150° (Gómez de Castro 1993; Hirth et al. 1994) and has been imaged recently with adaptive optics by Dougados et al. (2000) in [S II] but not in [O I]. Dougados et al. did image the bright emission knot HH 220 in [O I] at a distance of about 3″ from the star (§ 3.4).

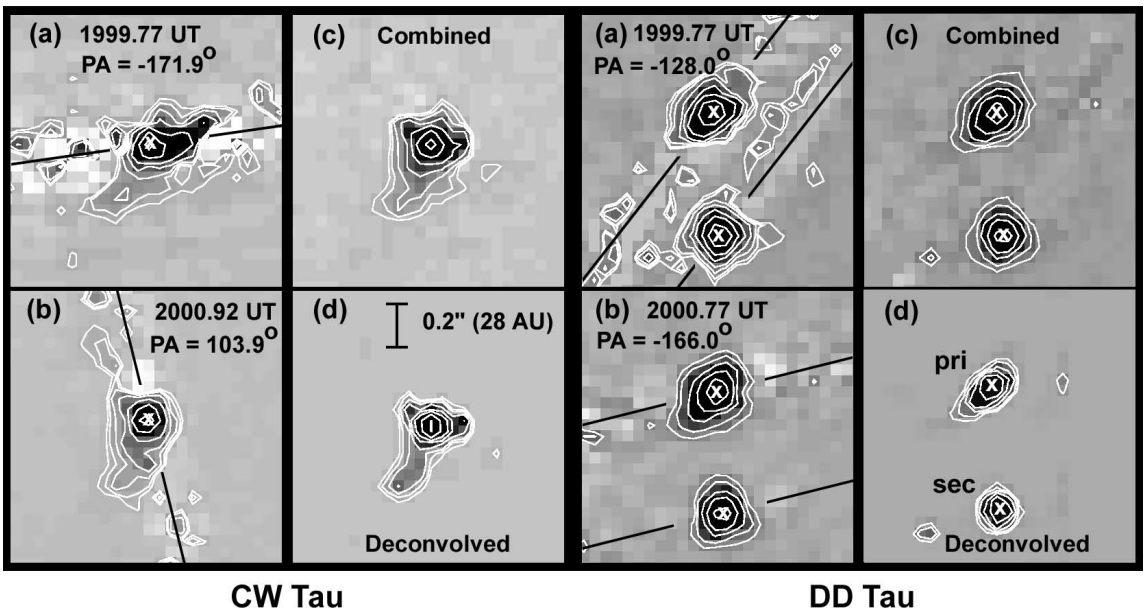

Fig. 2.—Emission-line images of [O I] λ6300 for the classical T Tauri stars CW Tau and DD Tau. (*a*, *b*) Slitless images with the stellar continuum removed, taken about a year apart. A cross marks the location of the star, determined from the stellar spectrum, which is oriented along the solid lines. The images are all rotated so north is up and east to the left. The P.A. listed is the direction on the sky perpendicular to the dispersion axis (the P.A. of the slit in long-slit spectra). The combined images (*c*) average the two epochs after masking out the noise from the stellar subtraction, as shown in Fig. 1. Masks are 4–5 pixels wide in all cases. The deconvolved images (*d*) used the STSDAS Lucy algorithm with *niter* = 8. Contour levels are described in Fig. 1.

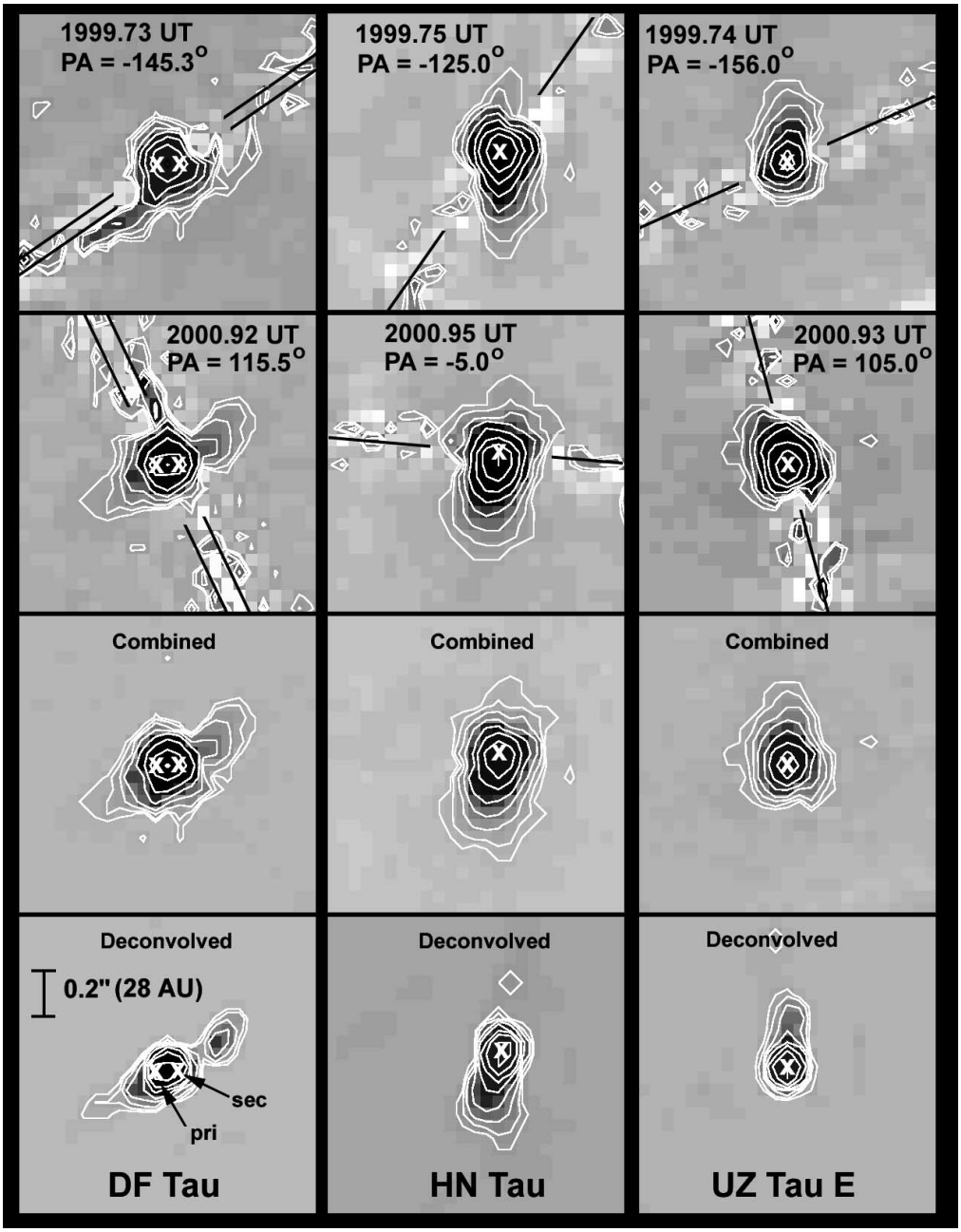

FIG. 3.—Same as Fig. 2, but for DF Tau, HN Tau, and UZ Tau E.

We were unable to orient the telescope to direct the jet perpendicular to the stellar spectrum, because of scheduling constraints with *HST*. However, the image taken at 2000.92 UT clearly shows that [O I] λ6300 extends to the southeast in a jet (Fig. 2). The first epoch also shows the jet, but less clearly, because the orientation was less favorable.

The spatial profile of CW Tau taken from the combined image along the axis of the jet, in Figure 4, shows a bright component that appears as a point source centered on the star, but there is also a knot of emission at a projected separation of $\sim$45 AU from the star. This knot comes mainly from the 2000 image, as much of the jet is masked out in the 1999 epoch. The clumpy nature of the CW Tau jet suggests a variable ejection at the source; in fact, CW Tau is the most variable source in our sample (Table 2), with the continuum at 6300 Å about a magnitude fainter in the 2000 image than in the 1999 image.

The 1999 image also shows a peculiar extension to the west that is not reproduced in the 2000 image. Whether or not the source is a close binary is unclear; Gómez de Castro (1993) also found CW Tau to extend in the east-west direction, but no companions were uncovered in the searches of Ghez et al. (1993) or Leinert et al. (1993). The star appears to have been accreting more rapidly in the fall of 1999 than it was one year later. In addition to being brighter, the 1999 spectrum of CW Tau is bluer than the one taken in 2000, as expected for a higher accretion rate. While the total flux in the stellar line He I λ5876 remains constant to within the uncertainties between the two epochs, the equivalent width of the Na D absorption doublet, a diagnostic of accretion and outflow, was

TABLE 2
[O I] λ6300 Equivalent Widths and Fluxes

Name	UT Date	EW([O I])[a] (Å)	$F_{[O\ I]}$[b]	F_{cont}[c]
CW Tau.....	1999.77	0.4 (0.2)	0.6 (0.3)	28
	2000.92	1.7 (0.3)	1.1 (0.2)	11
DD Tau pri.....	1999.77	1.6 (0.3)	0.49 (0.09)	2.9
	2000.77	2.5 (0.3)	0.59 (0.07)	2.4
DD Tau sec.....	1999.77	7.5 (0.9)	0.45 (0.05)	0.60
	2000.77	13.1 (1.0)	0.54 (0.04)	0.42
DF Tau.....	1999.73	0.8 (0.2)	3.1 (0.7)	37
	2000.92	0.8 (0.2)	3.0 (0.7)	36
HN Tau.....	1999.75	4.4 (0.3)	3.8 (0.3)	7.9
	2000.95	4.9 (0.3)	4.2 (0.3)	9.7
UZ Tau E[d].....	1999.74	1.3 (0.3)	2.0 (0.5)	15
	2000.93	1.4 (0.3)	2.6 (0.6)	18

Note.—Measured in a 0.″51 aperture centered on the star, except for DD Tau, where the aperture was 0.″36.
[a] Emission equivalent width of [O I] λ6300 (and errors).
[b] Observed (not dereddened) flux of [O I] λ6300 (and errors), in units of 10^{-14}ergs cm^{-2} s^{-1}.
[c] Observed continuum flux at [O I] λ6300, in units of 10^{-15} ergs cm^{-2} s^{-1} Å^{-1}. Uncertainties in the fluxes are 10%.
[d] Values refer to the combined spectrum of the primary and secondary.

more than twice as large in the first epoch than it was in the second epoch.

3.1.2. *DD Tau*

DD Tau consists of a pair of M3.5 classical T Tauri stars with strong forbidden lines in both the primary and secondary. The pair is separated by 81 AU (0.″58; Table 1) on the sky and is easily resolved with our data, although it is more difficult to subtract continuum because of the two bright stellar spectra in close proximity.

Figures 2 and 4 show that the primary has a weak [O I] λ6300 jet at P.A. ∼125°. DD Tau has some redshifted [O I], in addition to the dominant blueshifted component in 4 m echelle spectra (HEG95). However, the spatial profile on the opposite side of the jet of the primary in Figure 4 falls off with distance like a stellar point source, so there is no evidence for a counterflow in these images. The [O I] λ6300 line appears close to a point source for the secondary of DD Tau in Figures 2 and 4.

3.1.3. *DF Tau*

DF Tau is another classical T Tauri pair, with spectral types M2.0 and M2.5. The system is near the spatial resolution of *HST*, with a projected separation of 15 AU (0.″11). Substantial orbital motion has been observed over the last decade. A recent solution for the orbit shows a period of 93 yr, with $e = 0.5$ and $i = 135°$ (Tamazian et al. 2002). Spectra of the primary and secondary, including emission-line strengths for each, are discussed by Hartigan & Kenyon (2003). The stars are not cleanly separated in the current data set, so the equivalent widths and fluxes in Table 2 refer to the combined light of the pair.

In Figures 3 and 4, [O I] extends along a P.A. of ∼127° on both sides of the binary. It is possible that this is a single jet from one or both of the stars and that we are observing both sides of the flow. High-resolution ground-based spectra show both redshifted and blueshifted [O I] in this object (HEG95). The other possibility is that both stars drive jets and that these jets are parallel to one another. Accretion disks drive jets perpendicular to the disk plane, so parallel jets imply aligned disks, and therefore aligned rotation axes, for the two stars, an important constraint on binary formation.

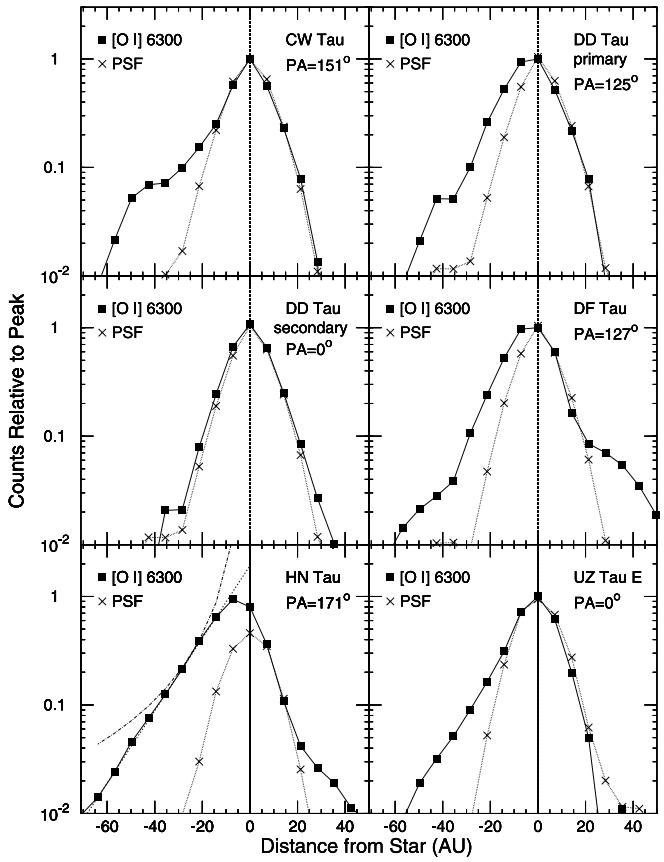

Fig. 4.—Spatial profiles of the [O I] λ6300 emission line, measured in a 5 pixel aperture along the direction of the jet at the P.A. listed for the combined images in Figs. 2 and 3. Squares show the observed profiles, while crosses show the expected PSF of any unresolved stellar component, calculated using the Tiny Tim algorithm. The counts are normalized to unity at the peak of the [O I] profiles. With the exception of the DD Tau secondary, all stars have a jet. DF Tau and HN Tau show jets on both sides of the star, while CW Tau has a distinct knot at a projected distance of ∼45 AU. Note that the *y*-axis has a logarithmic scale. The line drawn on the HN Tau profile, $I \sim \exp(-r/13.0)$, fits the observations better than the r^{-2} law, shown as a curve.

It will be difficult to distinguish between these alternatives for DF Tau, because the binary is near the resolution limit of *HST*; if there were two parallel jets, they would be unresolved spatially. If each star drives a jet, then the bases of these jets should follow the stellar positions as the two stars orbit one another, and there could be morphological changes of the jet over an orbit.

3.1.4. *HN Tau*

HN Tau has the most spatially extended jet of all the objects in our sample. The jet emits from the star out to 0.″5 along P.A. ∼171° in Figures 1 and 3. A faint counterjet also exists in this system (Fig. 4). Because the forbidden lines in HN Tau are bright in absolute terms and also have a large equivalent width, so the contrast of the line relative to the continuum is high (Table 2), the system is an excellent place to study emission-line ratios in the flow close to the star. The 2000.95 UT observations are particularly useful in this regard, as the dispersion direction was nearly perpendicular to the jet for those exposures. We discuss the emission-line ratios of this system in § 3.3.

3.1.5. *UZ Tau E*

UZ Tau E is a spectroscopic binary, with an inclination of about 60° and a separation of about 0.15 AU (Prato et al. 2002). The components of UZ Tau E have spectral types M1 and M4, a mass ratio of about 0.29, and a period of 19 days (Prato et al. 2002). UZ Tau E is a strong millimeter continuum source and also has CO that elongates along P.A. = 19°, similar to the direction of polarization (Jensen et al. 1996; Bastien 1985; Tamura & Sato 1989). The slitless image of UZ Tau E in Figure 3 shows that a jet emerges almost due north from the system. There is no evidence for a counterjet or for a second jet at any other P.A.. The star was accreting more in the 1999 epoch than in 2000—the TiO bands are more veiled in the first epoch, and Na D appears as an absorption feature with an equivalent width of 2.8 ± 0.2 Å in that spectrum. The Na D feature is absent at the 0.2 Å level in the 2000 epoch.

Jensen et al. (1996) interpret the CO as arising in a rotating disk, but if this explanation is correct, then the optical jet is ~70° away from the perpendicular to the disk. Instead, it may be that the CO does not trace the disk alone but becomes heated along the periphery of the jet as well, particularly to the south of UZ Tau E, where there is redshifted CO. Improved spatial resolution of the CO data is necessary to resolve this issue.

A companion binary named UZ Tau W, located some 3.″5 to the west of UZ Tau E, has a separation of 51 AU, with spectral types M2 and M3, and a mass ratio of 0.84 (Hartigan & Kenyon 2003). Both components of UZ Tau W are classical T Tauri stars, but the mid-IR and millimeter continuum is substantially less than it is in UZ Tau E (Ghez et al. 1994; Jensen et al. 1996), suggesting that the stars clear a gap in the disk of this system. Only the secondary shows any forbidden-line emission in the STIS spectra of Hartigan & Kenyon (2003), and these lines are too weak to image with the slitless data discussed in this paper. The Hα lines in the primary and secondary of UZ Tau W are bright but show no indication of any jets in the 1999 data (the 2000 images of the primary and secondary of UZ Tau W overlap and cannot be used to identify flows).

3.2. *Jet Collimation*

The degree of collimation of jets is one of the main observational constraints on theoretical models of outflows. If the ambient medium collimates the jet, the flow will have a wide opening angle close to the star until lateral ram pressure from the jet balances the pressure from the external medium (Cantó & Rodríguez 1980). In contrast, the opening angle of a freely expanding supersonic jet whose initial bulk motion is along a single direction is fixed by the Mach number of the flow, being larger for lower Mach numbers. Magnetic fields help to confine jets in disk wind models, so quantifying how the flow expands also constrains these models (Garcia et al. 2001; Shang et al. 1998). The situation is less clear for the real case of episodic flows, where collisions between subsequent ejections cause material to expand perpendicular to the axis of the flow. For this reason it is important to measure opening angles as close to the sources as possible.

The width of the jet at the base of the flow is another parameter predicted by jet models. Even if this width is unresolved, one can project the opening angle of the jet back to the source to see if the data are consistent with a constant opening angle emerging from a point source. If not, a nonzero projected jet width at the source implies either that the source region has a nonzero width or that the jet is less collimated close to the star. It is important to keep in mind that observations only constrain the opening angle and source regions of the portion of the flow that emits line radiation.

Observing how well jets collimate close to the star has been difficult because of the small spatial scales involved. Disks are typically 100 AU in size, and the collimation occurs on smaller scales. Resolving 15 AU scales for even the closest sources requires ~0.″1 spatial resolution, difficult to achieve from the ground, especially in the optical, where the brightest lines emit. Many jets are unsuitable for such studies, because of bow shocks that complicate measurements of widths close to the star, and because extinction from the disk obscures many jets close to their sources.

Using WFPC2 on *HST*, Ray et al. (1996) and Burrows et al. (1996) found the jet in HH 30 ($d = 140$ pc) to have an opening angle of about 3°. The jet is unresolved within ~50 AU of the star, but Ray et al. (1996) conclude that the projected jet width at the source is large (~30 AU), so the jet must be much less collimated close to the star. Ground-based measurements of jet widths valid at distances larger than 0.″4 for RW Aur, CW Tau, and DG Tau, reported by Dougados et al. (2000), indicate opening angles of a few degrees and jet widths of ~30 AU. Recent *HST* observations of jets using slit mapping with STIS for DG Tau and RW Aur, presented by Woitas et al. (2002), also show jets that expand away from their stars with opening angles of ~28° and ~5°, respectively. These jets are also unresolved near their sources, but they may have nonzero projected widths at the source of ~10 AU.

Slitless images remove continuum better than even the best narrowband images and for this reason are an excellent way to measure jet collimation, provided that (1) the jet emerges perpendicular to the dispersion direction and (2) velocity widths in the jet are unresolved. The best image in our sample for collimation studies is the 2000 epoch of HN Tau, although the 1999 epoch of UZ Tau E also provides some data (Fig. 3). As discussed in § 3.1, the HN Tau jet is bright and extends clearly for ~0.″5 in [O I] λ6300, and the dispersion direction for the 2000 epoch is within a few degrees of being perpendicular to the outflow. The FWHM of the [O I] λ6300 emission in HN Tau is about 70 km s^{-1}, or 0.3 pixels at 6300 Å (HEG95). This velocity broadening is negligible compared to the spatial FWHM of STIS in slitless mode.

Plots of the FWHM, measured from a Gaussian fit to the HN Tau jet at [O I] λ6300, appear in Figure 5*a*. Errors in the measurements are dominated by uncertainties in the continuum level and are comparable to the size of the points in most cases. The jet is clearly resolved beyond 15 AU, but the two closest points are unresolved, possibly from a stellar or inner-disk component to the line profile. The image used for the FWHM measurements was not rotated or shifted by fractional pixels at any time during the data reduction; such operations could, in principle, broaden the profiles as they interpolate counts between pixels.

There are several ways to correct for the instrumental spatial PSF of the STIS. To obtain a lower bound to the instrumental FWHM, we generated a theoretical PSF from the Tiny Tim routine, developed at STScI by Krist and Hook, and found an FWHM of 1.81 pixels (each pixel = 7.1 AU) at 6300 Å. We can improve on this estimate by measuring the PSF directly from the images. The FWHM of the PSF in the continuum near 6300 Å, measured along the direction of

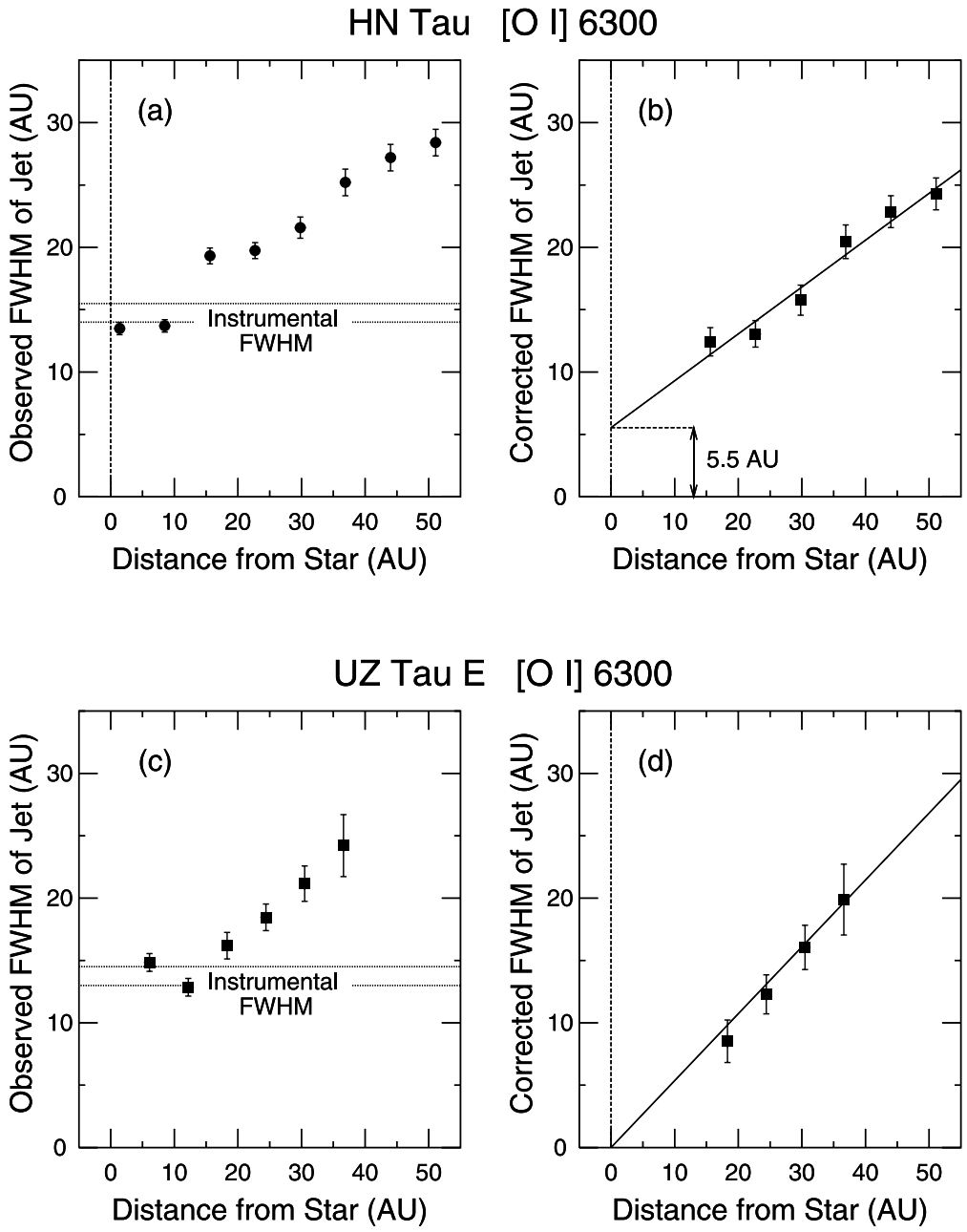

FIG. 5.—Spatial FWHM of the jets in HN Tau and UZ Tau E in [O I] λ6300. Dashed horizontal lines in (*a*) and (*c*) mark the $\pm 1\ \sigma$ range of the instrumental FWHM measured from the stellar continuum. When extrapolated to the origin, the corrected FWHM measurements of HN Tau imply a nonzero jet width at the source of a few AU. The line drawn through the points in (*b*) is a best fit described in the text. The corrected UZ Tau E observations (*d*) are consistent with a point source to within the errors of measurement.

the jet, is 2.06 ± 0.08 pixels. The FWHM along the dispersion direction (perpendicular to the jet) should increase to 2.08 ± 0.10 pixels, taking into account the velocity width in the [O I] line described above.

Correcting the observed FWHM for the instrumental broadening leads to the plot of intrinsic FWHM versus distance in Figure 5*b*. The error bars in this figure derive from measurement errors in the observed FWHM and the instrumental PSF. The result is remarkably linear, with a slope of 0.38 ± 0.04 and a y-intercept of 5.5 ± 1.4 AU. Hence, if the opening angle of the jet stays constant close to the source, as it does farther out, the jet has a nonzero width at the source at about the 3 σ level. This width is small, about the size of the asteroid belt in our solar system. Alternatively, the jet could originate from a smaller region and have a somewhat wider opening angle close to the source.

The full opening angle of the jet in HN Tau of $21^\circ \pm 2^\circ$ is quite wide; at larger distances from the source, the brightest jets usually have opening angles of only a few degrees (Reipurth & Bally 2001). However, as pointed out by the referee, the width of the RW Aur jet measured by Woitas et al. (2002) at a projected distance of 56 AU from the star is $\sim$14 AU, after correction for the PSF. Assuming that the jet originates from a small source region, this width implies an opening angle of 14°, comparable to what we observe in HN Tau. The true opening angle is smaller than that observed by a factor of $\sin i$ for narrow opening angles. The HN Tau flow is blueshifted by $\sim$140 km s^{-1} and therefore has a

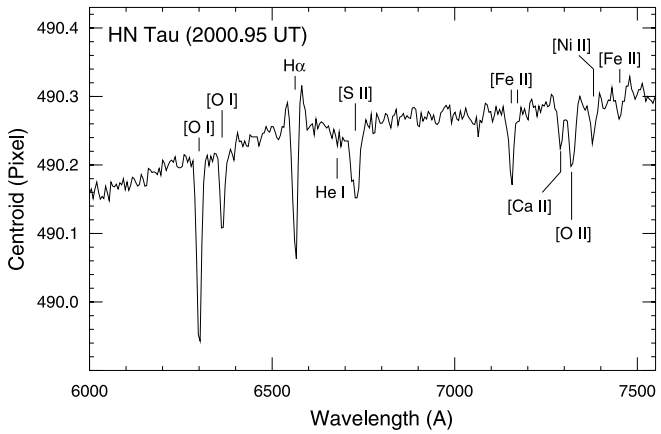

FIG. 6.—Position centroids of HN Tau for the 2000 epoch, measured using a 21 pixel aperture centered on the stellar position (this is not an absorption-line spectrum). We use this plot to identify emission lines in the jet, which will have lower centroids (smaller y-values) than stellar lines or continuum. The spikes on either side of Hα are caused by a bright halo that surrounds this line, which is saturated in our images. The centroids gradually increase with wavelength because the spectrum tilts slightly on the CCD. Individual emission lines are discussed in the text; the feature marked as [O II] is a blend of four [O II] lines and a [Ca II] line.

component of motion out of the plane of the sky, but without knowing proper motions we cannot determine the inclination. For a freely expanding flow, the observed opening angle implies a Mach number of $\sim 5.4/\sin i$; Mach numbers of 20–40 are typical among stellar jets.

Plots of the FWHM of the UZ Tau E jet appear in Figures 5*c* and 5*d*. This jet is fainter than the one in HN Tau and does not emerge perpendicular to the stellar spectrum for either epoch (Fig. 3). Nevertheless, the 1999 epoch is usable for FWHM measurements, although traces perpendicular to the jet involve interpolation across pixels in the original data. The instrumental FWHM is 1.94 ± 0.1 pixels for UZ Tau E, somewhat smaller than for HN Tau. Like the HN Tau jet, the jet in UZ Tau E increases in width as it moves away from the star, with a full opening angle of about 30°. However, UZ Tau E shows no evidence for a nonzero jet width at the source.

3.3. *New Emission-Line Diagnostics in T Tauri Jets: HN Tau*

3.3.1. *Emission Centroids and Line Images*

Emission lines are the primary way to probe physical conditions in jets. Unfortunately, standard density diagnostics, such as the [S II] λ6716/λ6731 ratio, are typically in the high-density limit when the jet is close to the star. We can use our slitless data to identify emission lines in the jet that may prove useful as measures of the density, temperature, and ionization state in the regions where the normal diagnostics fail.

In slitless images, lines in jets shift the centroid position of that wavelength spatially with respect to the position of the star at continuum wavelengths. Once the emission lines are identified by this shift, the challenge is to extract flux ratios as a function of position. This latter task is far more difficult than identifying lines. Centroid shifts only show that the line emission occurs in the jet and do not uniquely determine the spatial distribution of the emission.

The plot of centroids for the 2000 epoch of HN Tau in Figure 6 shows that these offsets have noise at the level of only 0.01–0.02 pixels, or about 1% of the FWHM of the PSF. The emission lines of [Fe II] and [Ni II] in the figure have not been seen before in jets at subarcsecond distances from their stars. Some of these emission lines have high enough signal-to-noise ratios (S/Ns) to make images worthwhile, and we present these in Figure 7. As expected for a low-density medium, forbidden lines dominate in the jet, while permitted lines are the brightest at the star.

There are three broad categories of emission lines in Figure 7. As the contours show, the Ca II triplet around 8500 Å and permitted lines, such as Fe II λ6516, are situated exactly on the star and are unresolved spatially. A second group of lines emits primarily in the jet. These are forbidden lines such as [O I] λ6300, the red [S II] doublet (blended in these data), a blend of four [O II] lines and two [Ca II] lines near 7320 Å, and the forbidden lines of [Fe II], such as those at 8617, 7155, and 7173 Å.

A third group of lines emits primarily at the star but extends very weakly along the jet near the level of detection with this technique. These include O I λ8446, He I λ5876, and He I λ6678. The extensions along the jet are very subtle for these lines (Figs. 7 and 8) and would be easy to dismiss as instrumental were it not for the near-perfect symmetry of the PSF and permitted lines, such as Ca II λ8662. The stellar PSF clearly dominates in these images; any flux ratio images must await better spatial resolution. But these observations provide a glimpse as to what will become possible to measure eventually with larger space telescopes.

Flux ratios of most of the forbidden lines in the HN Tau jet are shown in Figure 8. The ratios are uncorrected for reddening and are normalized to unity at the peak of the [O I] λ6300 emission. The [S II] $\lambda\lambda$6716+6731/[O I] λ6300 ratio decreases close to the star, as expected if the electron density in the jet rises closer to the star. The critical densities increase from $\sim 10^4$ cm^{-3} for [S II], to $\sim 10^6$ cm^{-3} for [O I] λ6300.

3.3.2. *The* [O I] λ5577/λ6300 *Ratio*

The observed ratio of [O I] λ5577/λ6300 is important because it constrains the electron density close to the star. The λ6300 line is one of the defining characteristics of classical T Tauri stars in ground-based spectra at echelle resolution, and the weaker λ5577 line is also present in most stars (HEG95). Both lines frequently show two kinematic components, a high-velocity component arising in the jet at some distance from the star and a low-velocity component that might arise at the base of the jet or a disk wind. It has recently been shown that λ5577 does not partake of the orbital motion in spectroscopic classical T Tauri binaries, indicating that this line originates in outflowing material at some distance from the star (M. Huerta et al. 2004, in preparation). High spectral resolution observations are essential for ground-based observations to separate T Tauri star emission from the bright terrestrial airglow line, and they also make it possible to remove all the photospheric features from the vicinity of the emission-line profile. Our *HST* spectra have no airglow, but the low spectral resolution makes it more difficult to identify the continuum level and correct for the presence of weak photospheric absorption lines.

The [O I] λ5577 line in our 2000 epoch of HN Tau has a signal at the same level as residual photospheric features, about 0.4 Å in equivalent width, when extracted from a 3 pixel aperture centered on the star. This is a factor of 10 lower than the equivalent width of [O I] λ6300, 3.9 ± 0.3 Å measured over the same aperture. The spatial position is within $\sim 0\farcs1$ of the stellar position for HN Tau; any extension along the jet is impossible to see in our data, because the line is too weak. For comparison, HEG95 measured the equivalent widths of

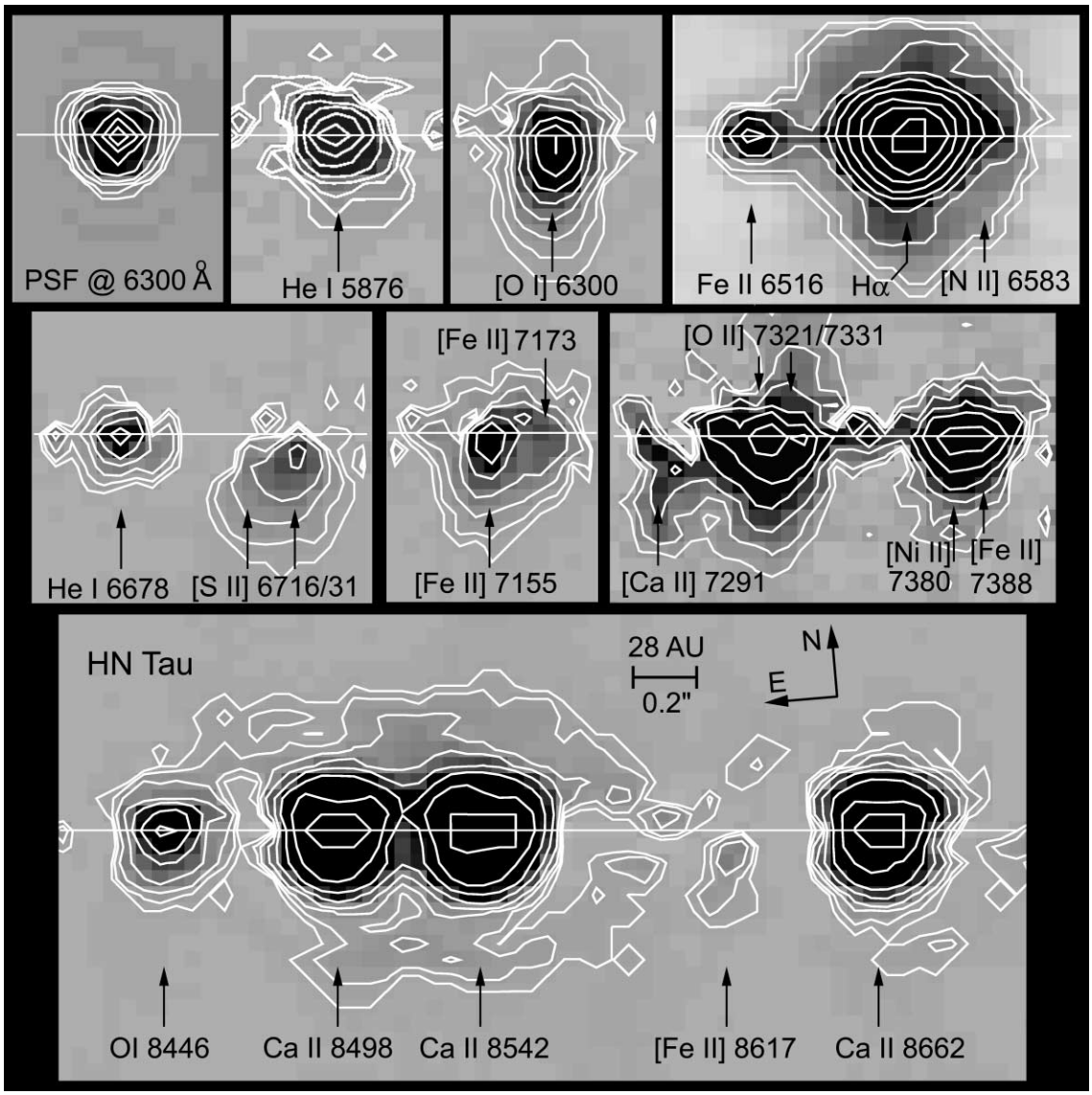

FIG. 7.—Images of emission lines in HN Tau, taken from the 2000 epoch. The horizontal line denotes the stellar position measured from the continuum, which has been subtracted from these data. Adjacent contours differ by a factor of 2 and range from 20 to 2560 ADU for all images except He I λ5876, where the lowest contour is 10 ADU. A level of 20 ADU ranges from 3.2×10^{-17} ergs cm^{-2} s^{-1} pixel^{-1} at [O I] λ6300 to 5.6×10^{-17} ergs cm^{-2} s^{-1} pixel^{-1} at Ca II λ8662.

[O I] λ5577 and [O I] λ6300 emission in a 2″ aperture centered on HN Tau to be, respectively, 0.59 ± 0.07 and 7.50 ± 0.10 in the low-velocity component, while the corresponding total equivalent widths are 0.77 ± 0.11 for λ5577 and 13.2 ± 0.40 for λ6300. The [O I] λ5577/λ6300 ratio increases closer to the star, because the critical density is higher for the λ5577 line than it is for the λ6300 line. Hence, an equivalent width close to the star of 0.4 Å for [O I] λ5577, roughly 10% of that for [O I] λ6300, is in line with ground-based results.

When dereddened, the HEG95 [O I] λ5577/λ6300 ratio is 0.057 ± 0.009, if we use the entire line profile, and 0.078 ± 0.013, if we use only the low-velocity component, which emits closer to the star (Hirth et al. 1997). The uncertainties in these estimates are dominated by a generous uncertainty in the reddening of ± 1 mag at V. In what follows, we adopt 0.08 ± 0.03 for the [O I] λ5577/λ6300 line ratio. The average distance from the star within a 3 pixel aperture centered on the star is 0.75 pixels, or $\sim$5 AU.

Diagnostic curves for the [O I] λ5577/λ6300 ratio as a function of electron density and temperature for a five-level atom appear in Figure 9*a*. These curves use collision strengths, Einstein A-values, and energy levels compiled by the CHIANTI project (Dere et al. 1997; Young et al. 2003) for ions and by Pradhan & Peng (1995) for neutrals. The observed [O I] λ5577/λ6300 ratio implies $\log N_e = 6.3 \pm 0.2$ if $T = 10,000$ K. The electron density rises to $\log N_e = 7.6$ if the temperature drops to 5000 K. The uncertainty in the electron density is dominated by the uncertainty in the temperature and not by errors in the reddening or in the observed line ratio.

We ran several radiative shock models (see Hartigan et al. 1994) to determine a characteristic temperature for [O I] line emission in low-velocity shocks. In a 40 km s^{-1} shock with a neutral preshock medium of density 10^6 cm^{-3}, half of the [O I] λ6300 arises from regions where the temperature lies between 7980 and 5300 K. If half the preshock gas is ionized, the numbers become 7060 and 5010 K, respectively, while the corresponding values for an 80 km s^{-1} shock into neutral material for a preshock density of 10^3 cm^{-3} are 9950 and 6200 K. Taking 6500 ± 1000 K as the emitting temperature for postshock [O I] in these systems, Figure 9*a* shows that the

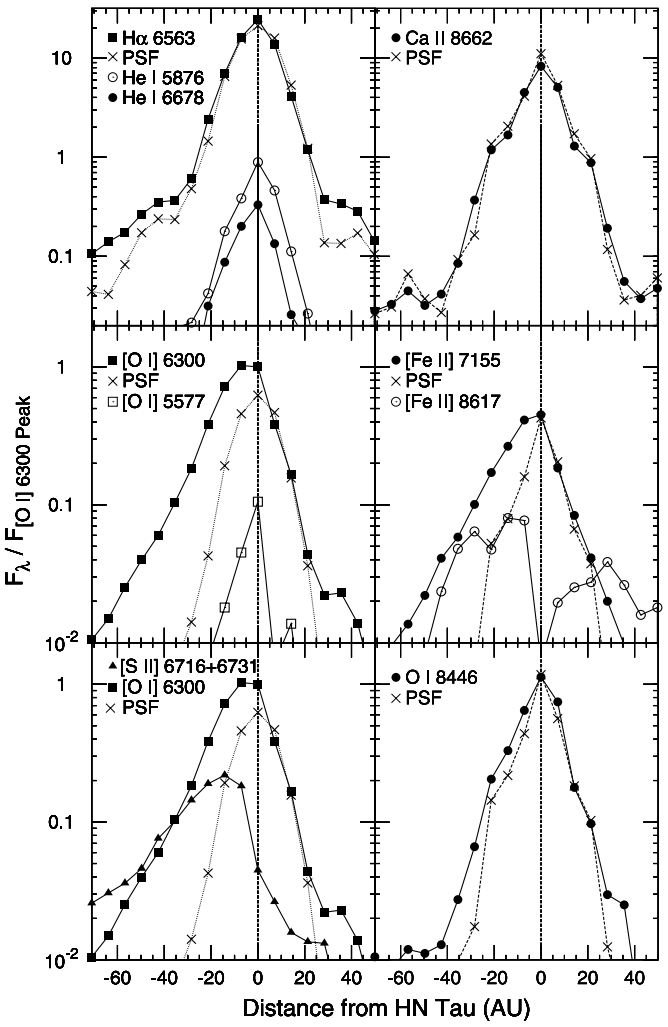

FIG. 8.—Like Fig. 4, but for spatial profiles of various emission lines along the HN Tau jet, measured from the 2000 epoch. The units on the *y*-axis are flux ratios, normalized to the peak value of [O I] λ6300 and not dereddened. Several lines have a strong stellar component. The PSFs shown are centered on the star, normalized to fit under the observed profiles. Differences between the PSFs and the observations indicate extended nonstellar emission. Uncertainties in the *y*-values are 0.01, except for [Fe II] λ8617, where they are ~0.02.

electron density in the jet close to the star (~5 AU) becomes $\log N_e = 6.95 \pm 0.4$.

3.3.3. [Fe II] *λ7155/λ8617 as a Density Diagnostic*

The most important new emission lines identified in the HN Tau jet near the star may be [Fe II] λ8617 and [Fe II] λ7155. Their ratio is an excellent density diagnostic when $6 \lesssim \log N_e \lesssim 7.5$, because the upper levels of the two transitions have similar energies, but the Einstein *A*-value of 0.0356 s^{-1} for λ8617 is about a factor of 4 lower than the value of 0.146 s^{-1} for λ7155 (Bautista & Pradhan 1998). The diagnostic curves of Bautista & Pradhan (1996) show that the [Fe II] λ7155/λ8617 ratio rises from its low-density limit of ~0.7 when $\log N_e \sim 5.8$, to more than 4.0 when $\log N_e > 7.2$. In the high-density limit, the ratio approaches 4.86.

One possible issue in using forbidden lines of Fe II as density diagnostics is that fluorescent pumping via permitted transitions to electronic levels alters the forbidden-line spectrum when the electrons cascade back toward the ground state (Rodríguez 1999). However, fluorescence affects fluxes from lines like λλ8617 and 7155, which originate from lower energy levels, by less than 10%, even in a photon-rich environment like the Orion Nebula (Verner et al. 2000), so fluorescence should not be important for these transitions in stellar jets.

The main uncertainty in the [Fe II] λ7155/λ8617 ratio for our target objects comes from the stellar continuum near 8617 Å, which is difficult to measure because of halos in the PSF that accompany the extremely bright Ca II triplet (Fig. 7). Also, the weak Pa 14 λ8598 line at the stellar position contaminates [Fe II] λ8617 in our spectra close to the star. Hence, uncertainties in the fluxes for the [Fe II] λ8617 profile in Figure 8, determined by choosing different continuum subtractions, are 0.02–0.03, a factor of 2 higher than for the other profiles. The [Fe II] λ7155 line is also affected on its red end by the weak [Fe II] λ7173 feature (Fig. 7).

We extracted spectra at several locations along the flow, fitting the continuum and deblending the fainter lines using the *splot* command in IRAF. Despite the nearby bright lines and the Paschen blend, [Fe II] λ8617 is easy to see in the spectra between about +15 and +40 AU. There is also weaker [Fe II] λ8617 emission on the redshifted side of the flow, but the S/N is lower there for both this line and the [Fe II] λ7155 transition. Within 10 AU of the star, the Ca II triplet and Pa 14 line make it impossible to measure a reliable flux for [Fe II] λ8617. Using a 3 pixel (21 AU) aperture at distances of 16, 23, and 30 AU from HN Tau, we find the dereddened [Fe II] λ7155/λ8617 ratio to be 2.0 ± 0.4, 1.7 ± 0.3, and 1.6 ± 0.3, respectively. The corresponding electron densities from the curves of Bautista & Pradhan (1996) are $\log N_e = 6.35 \pm 0.15$ at 16 AU, α at 23 AU, and 6.2 ± 0.15 at 30 AU. These electron densities are consistent with those inferred indirectly from the [O I] and [S II] lines discussed above.

Other transitions from the $a\ ^2G$–$a\ ^4F$ levels of Fe II include lines at 7453 and 7173 Å, both observed in HN Tau, and that at 7388 Å, which is blended with a [Ni II] transition at 7378 Å. All of these lines extend in the jet (Figs. 6 and 7) but are weaker than [Fe II] λ7155.

3.3.4. *The Auroral* [O II] *Doublets and Ionization Fractions*

In order to measure a mass-loss rate, we must know the ionization fraction $X = N_{\rm H\,II}/(N_{\rm H\,II} + N_{\rm H\,I})$ of the gas as well as the electron density. The ionization fraction is fixed by heating and cooling within the flow and so constrains wind launching mechanisms. Ionization fractions in bright stellar jets like HH 111, HH 34, and HH 47 range from 3%–6%, although somewhat higher ionization fractions of ~20% are seen in fainter jets like HL Tau and HH 24 (Hartigan et al. 1994; Bacciotti & Eislöffel 1999). These values refer to cooling zones behind shocks in the flow at least 100 AU, and often several hundreds of AU, from the star. If these cooling zones are unresolved, the ionization fraction measured from the line emission refers to an average over the emitting zone.

Because the ionization states of both oxygen and nitrogen are tied to that of hydrogen through charge exchange (Bacciotti & Eislöffel 1999), the [N II] λ6583/[O I] λ6300 ratio gives a good measure of the ionization fraction, as long as these gases emit at the same temperature over the region being measured. Unfortunately, [N II] λ6583 is blended with Hα in our spectra, so we cannot use this diagnostic.

However, the density is high enough close to the star to make the auroral lines in [O II] visible, and we can use these lines, together with the [O I] lines, to measure the ionization

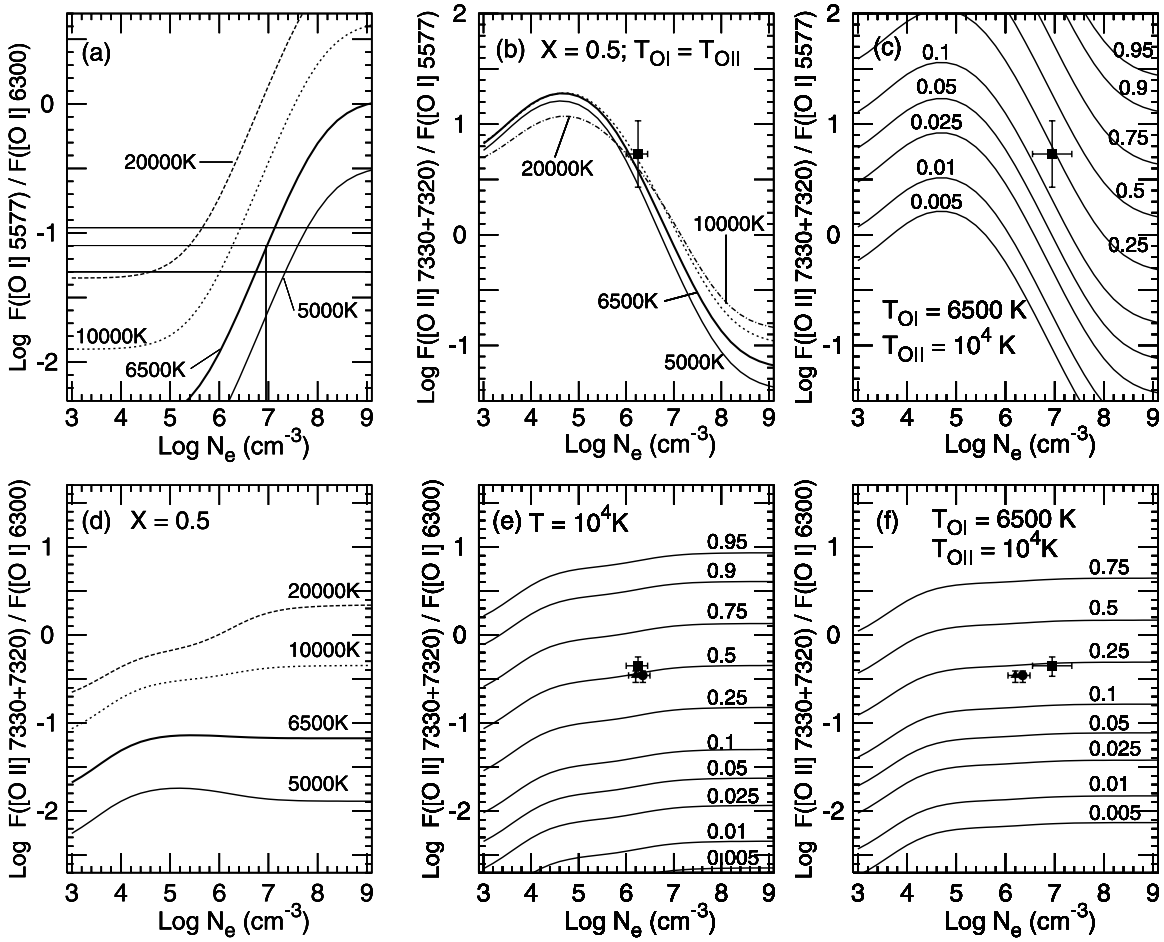

FIG. 9.—Temperature, density, and ionization fraction diagnostic diagrams for forbidden lines in jets. (*a*) The [O I] line ratio $\lambda5577/\lambda6300$ depends on both temperature and density. The thick curve is for the typical temperature of [O I] emission in postshock gas. The horizontal lines mark the observed and ±1 σ values for the ratio observed close to HN Tau, which implies a density of $\sim10^7$ cm^{-3}. (*b*) The ratio of the red [O II] quartet to [O I] $\lambda5577$ is insensitive to density for a fixed ionization fraction. The point, discussed in the text, assumes that both O I and O II emit at 10^4 K. (*c*) Same as (*b*), but curves are shown for a variety of ionization fractions with $T_{O\,II} = 10^4$ K and $T_{O\,I} = 6500$ K, as appropriate for low-velocity radiative shocks. As in (*b*), the point is for the HN Tau jet about 5 AU from the star. (*d*) The [O II] $\lambda7325$/[O I] $\lambda6300$ ratio as a function of temperature and density for an ionization fraction of 0.5. (*e*) Same as (*d*), but for different ionization fractions at 10^4 K. The triangle, circle, and square are for positions in the jet 30, 16, and 5 AU from the star, respectively. The densities for the triangle and circle were determined from [Fe II] line ratios and that for the square from the [O I] $\lambda5577/\lambda6300$ ratio, as described in the text. (*f*) Same as (*e*), but for temperatures appropriate for shocked gas. These plots show that the HN Tau jet has a substantial ionization fraction within 50 AU of the star.

fraction in the gas. This ratio has the advantage of being independent of the elemental abundances. The auroral [O II] lines, which arise from transitions from the ^2P levels at 5.02 eV above ground to the ^2D levels at 3.33 eV, consist of a closely spaced pair at 7321 Å and another pair at 7331 Å. All four lines are blended in our spectra, but this is not a problem, because we wish to measure the sum of the fluxes in the entire multiplet.

3.3.4.1. Correcting the Red [O II] *Blend for* [Ca II] *λ7324 Using* [Ca II] *λ7291*

Unfortunately, [Ca II] $\lambda7324$ also contributes to the four lines of [O II] in the $\lambda7325$ blend. The [Ca II] $\lambda7324$ line, together with its counterpart [Ca II] $\lambda7291$, come from the $3d\ ^2D_{5/2,\,3/2}$ levels to the ground state $4s\ ^2S_{1/2}$. The [Ca II] $\lambda7291$ line is easily resolved from the $\lambda7325$ blend in our spectra, so we would like to use it to remove the contribution of [Ca II] $\lambda7324$ from the [O II] auroral lines. To do this, we must consider how the [Ca II] $\lambda7291/\lambda7324$ line ratio behaves in the low-density limit (LDL), in the high-density limit (HDL), and when fluorescent pumping from the ground state populates the levels. The $3d\ ^2D_{5/2,\,3/2}$ levels are metastable and can be pumped by photoexcitation of the Ca II K and H lines from the ground state to $4p\ ^2P_{3/2,\,1/2}$, followed by decay to the $3d$ levels, a process responsible for the infrared triplet of permitted lines at 8497, 8538, and 8663 Å.

In the LDL the flux ratio [Ca II] $\lambda7291/\lambda7324$ equals the ratio of the statistical weights of the levels (3/2), with tiny corrections for temperature and photon energy. The LDL value of the ratio is 1.495. To calculate the ratio in the HDL requires the Einstein A-values for [Ca II] $\lambda\lambda7291$ and 7324. Barton et al. (2000) measured these with high accuracy and found the two values to be equal to within $\sim3\%$. For this reason, the HDL of 1.535 is nearly the same as the LDL for this line ratio. The critical density is $\sim5\times10^7$ cm^{-3}. Thus, to within a percent or two, when collisions from the ground populate the $3d$ levels the [Ca II] $\lambda7291/\lambda7324$ flux ratio will always be 1.5.

Next, consider the case in which fluorescent pumping of the $4p$ levels, followed by cascade to $3d$, dominates the production of [Ca II] $\lambda\lambda7291$+7324. For a flat continuum, the pumping of the K line is twice that of the H line. Using the gf-values compiled on a Web site maintained by R. Kurucz, we calculated the relative steady state populations of the $^2D_{5/2}$ and $^2D_{3/2}$ levels to be 1.49. Hence, in this case the [Ca II]

λ7291/λ7324 flux ratio is also $\sim$1.5. If more photons are available at K than at H for fluorescence, then the [Ca II] λ7324 flux diminishes relative to that of [Ca II] λ7291.

We now estimate the relative importance of collisions versus pumping for populating the 3*d* levels of Ca II in the HN Tau jet. At a distance of 10 AU from the star, the electron density is $\sim 3 \times 10^6$ cm^{-3}. The calculations of Chidichimo (1981) show that the collision strengths between 4*s* and 3*d* are about 0.24 of those between 4*s* and 4*p*. Pradhan & Peng (1995) quote a collision strength of 17.5 at 10^4 K for 4*s*–4*p*, so we take the total collision strength of 4*s*–4*d* to be 4.2. The spline fits of Burgess et al. (1995) give 4.3 for the collision strength between 4*s* and 4*p*. Hence, $\Omega_{7291} = 2.5$, and the rate of collisional excitation from the ground state to $^2D_{5/2}$ for each Ca II atom in the ground state is $\sim$0.075 s^{-1}.

The equivalent width of Ca II K in HN Tau is $\sim$50 Å, and the continuum flux is $\sim 3 \times 10^{-15}$ ergs cm^{-2} s^{-1} Å^{-1} (Valenti et al. 1993; Gullbring et al. 1998). A typical Ca II K line width is 300 km s^{-1} for classical T Tauri stars such as HN Tau, where the broad component of the emission-line profile dominates the flux (Alencar & Basri 2000), so a typical specific flux in the K line is $\sim 4 \times 10^{-14}$ ergs cm^{-2} s^{-1} Å^{-1}. Reddening is a large uncertainty at 3933 Å, with a correction factor varying from 13.4 when $A_V = 1.9$ (HEG95) to 2.4 if $A_V = 0.65$ (Gullbring et al. 1998). Taking the larger reddening, we obtain a mean intensity of 0.36 ergs cm^{-2} s^{-1} Å^{-1} sr^{-1}, or 1.85×10^{-12} ergs cm^{-2} s^{-1} Hz^{-1} sr^{-1}. The Einstein *B*-coefficient for Ca II K, where $gf = 1.36$, is 4.48×10^{10} erg^{-1} s^{-1} cm^2, so the pumping rate of Ca II K in the jet at 10 AU is 0.083 s^{-1} per Ca II atom in the ground state. The upper state of Ca II K branches to the $^2D_{5/2}$ with a probability of 0.063, so the rate per Ca II atom at which the $^2D_{5/2}$ level is populated by K fluorescence is $\sim$0.005 s^{-1}. The rate decreases if the reddening is lower.

Hence, collisions should dominate the population of the 3*d* level of Ca II at 10 AU, especially if the reddening is closer to the low value. In what follows we adopt an intrinsic flux ratio of 1.5 for [Ca II] λ7291/λ7324. The contribution of [Ca II] λ7324 to the red [O II] blend ranges from negligible at the stellar position, to $\sim$20% at 30 AU from the star. A recent echelle spectrum of HN Tau that resolves [Ca II] λ7324 from the [O II] lines at 7321 and 7331 Å was obtained at the request of the authors by C. Johns-Krull at McDonald Observatory (2004, personal communication) and shows the [Ca II] λ7291/λ7324 ratio to be equal to 1.5, with an uncertainty of $\sim$50%.

3.3.4.2. *Flux Ratios Involving the Auroral* [O II] *Lines*

As shown in Figure 9*b*, the ratio of the red [O II] lines to [O I] λ5577 is relatively independent of the temperature (provided the temperature is the same for O I and O II), because the energy difference between the ^2P O II levels and the ^1S O I state is only 0.83 eV ($kT = 0.86$ eV for $T = 10^4$ K). Hence, the ratio gives a direct measure of the ionization fraction if the density is known. Lower or higher ionization fractions simply shift the curves in Figure 9*b* down or up, respectively, according to the relative abundances of O II and O I. The abundances ratio O II/O I equals $\frac{8}{9}$ the abundance ratio H II/H I, the factor of $\frac{8}{9}$ resulting from the outlet channels of the charge exchange reaction (Osterbrock 1989, p. 43).

The flux ratio [O II] $\lambda\lambda$7321+7331/[O I] λ5577 in a 3 pixel aperture centered on the star, dereddened with $A_V = 1.9$ (HEG95), is 5.3 ± 2.6. The large uncertainty comes from the low S/N in [O I] λ5577. The point plotted in Figure 9*b* is for $T_{\rm O\,I} = T_{\rm O\,II} = 10^4$ K, so the density inferred from Figure 9*a* is $\log N_e = 6.25 \pm 0.2$ (the uncertainty determined from the limits on the observed line ratio in Figure 9*a* for $T = 10^4$ K). For this case of equal O I and O II temperatures, the ionization fraction is high, 0.5 ± 0.15.

The curves in Figure 9*c* show how the observed [O II]/[O I] ratio constrains the ionization fraction if the emission comes from shocks, where the characteristic temperature of O I is $\sim$6500 K and that of O II is $\sim 10^4$ K ([O II] λ7325 emits half of its light between 12,400 and 8200 K for a 40 km s^{-1} shock into neutral material with a preshock density of 10^6 cm^{-3}). Taking $\log N_e = 6.95$, as appropriate for $T_{\rm O\,I} = 6500$ K (Fig. 9*a*), the [O II] λ7325/[O I] λ5577 line ratio implies an ionization fraction of 0.25 ± 0.15.

The [O II] λ7325 blend is also useful when combined with [O I] λ6300. As seen in Figure 9*d*, this ratio is relatively independent of density but depends strongly on temperature. Even so, the ratio constrains the ionization fraction. We plot two cases, a constant temperature of 10^4 K for all lines (Fig. 9*e*) and a case appropriate for low-velocity shocks. The dereddened flux ratio of [O II] $\lambda\lambda$7321+7331/[O I] λ6300, measured in a 3 pixel aperture centered on HN Tau, is 0.45 ± 0.11. The uncertainty is dominated by the error in the reddening, assumed to be ± 1 mag at *V*. The dereddened flux ratio in 3 pixel apertures centered at 16 and at 30 AU are both 0.35 ± 0.06. These points are plotted in Figures 9*e* and 9*f*, where the densities are taken from Figure 9*a* for the stellar position and from the [Fe II] line ratios at 16 and 30 AU. The resulting ionization fractions are 0.50 ± 0.05, if the gas emits at 10^4 K, and 0.20 ± 0.05, if the emitting zone is like a typical postshock region. Either way, the strong [O II] lines in the HN Tau jet in Figure 7 imply that the flow has a substantial ionized component at distances of 5–35 AU from the star.

3.3.5. *Filling Factor and Mass-Loss Rate for the HN Tau Jet*

Estimates of mass-loss rates in stellar jets typically rely on forbidden-line luminosities and require an estimate of the electron density, the latter poorly known close to the star because the most common density tracer, the ratio of the red lines of [S II], is in the HDL there (Appendix A of HEG95). We can improve on previous work for HN Tau because the jet is resolved spatially, so our observations do not average variable quantities, such as the intensity and the density, over a large beam size and because the slitless spectra make it possible to follow the electron density and ionization fraction as they vary with distance from the source. The new measurements of the auroral lines of [O II] close to the star are particularly important for constraining shock models.

One way to visualize the jet is as a clumpy flow that fills some fraction *f* of the volume. In this case, the mass-loss rate at some position in the jet equals $N_e X m V A f$, where the electron density N_e, ionization fraction *X*, mass per nucleon *m* ($\sim m_{\rm H}$), velocity *V*, and cross-sectional area *A* of the jet are all known or measurable quantities and the filling factor *f* can be estimated from the brightness of the jet at [O I] λ6300. At a distance of 25 AU, the HN Tau jet has a diameter of 14 AU (Fig. 5) and $\log N_e = 6.2$. Taking the ionization fraction to be 0.50, appropriate for the isothermal cases in Figure 9*e*, the column density of neutral H along the line of sight through the jet is $\log N_{\rm H\,I} = 3.3 \times 10^{20}$ cm^{-2}. Assuming an O/H abundance of $\log(N_{\rm O}/N_{\rm H}) = -3.18$ and correcting for the factor of $\frac{8}{9}$ discussed at the beginning of § 3.3.4.2, the column density of neutral oxygen is 2.3×10^{17} cm^{-2}. For $\log N_e = 6.2$ and $T = 10,000$ K, the fraction of oxygen in the $^1D_2$ level

is 2.87×10^{-2}, so the column density of oxygen in this level is 6.6×10^{15} cm^{-2}. The intensity of the [O I] λ6300 line if the emission fills the entire volume of the jet should be 2.0×10^{-10} ergs cm^{-2} s^{-1} arcsec^{-2}. The observed [O I] λ6300 intensity in the middle of the jet at 25 AU, dereddened with $A_V = 1.9$, is 1.3×10^{-12} ergs cm^{-2} s^{-1} arcsec^{-2}, so the volume filling factor is 0.6%. The low filling factor in the jet cannot be caused solely by having the jet denser along its axis, because the width of the jet is resolved in the images. One can also explain the low filling factor with a model that has a smooth jet with a relatively hollow core or with a very clumpy flow.

The case of a shock front is somewhat different from the above discussion, because the hot postshock gas dominates the line emission, while all the gas, including the preshock gas and the cool postshock gas, contributes to the mass loss. If the cooling distance behind a shock in a jet is small relative to the width of the jet, then the total line emission from the jet will be small compared to what it would be if the beam were filled everywhere with hot, emitting material. Rather than describe the shocked flow in terms of a filling factor, which is an awkward concept for a shock, because gas of various densities can fill the entire beam even though only a fraction of it emits, it is more convenient to simply compare the emission-line ratios and fluxes expected from a shock with the observations.

HEG95 computed a grid of shock models of various densities and shock velocities in an attempt to explain the emission lines in jets. Their Figure 12 shows that although the line ratios are broadly consistent with a shock, the models underpredict the [S II] λ6723/[O I] λ6300 and [N II] λ6583/[O I] λ6300 ratios by 1–2 orders of magnitude for a given value of [O I] λ5577/λ6300. The points in Figure 9 clearly show how the models should be improved—the large auroral [O II] fluxes imply a high ionization fraction in the postshock gas that cannot be achieved by having a neutral preshock medium, as was assumed by HEG95.

While it is beyond the scope of this paper to calculate another grid of shock models, we found excellent agreement for both the observed fluxes and the line ratios for a model with a 40 km s^{-1} shock, a preshock ionization fraction of 0.7, a preshock magnetic field of 100 μG, and a preshock density of 2×10^5 cm^{-3}. Essentially, what happens is that the larger preshock ionization fraction increases the electron density in the cooling zone, so that lower velocity shocks like those observed from proper motions in jets (Hartigan et al. 2001) now match the line ratios and fluxes.

We obtain the following line ratios for the above model: $\log([\mathrm{O\,I}]\ \lambda5577/\lambda6300) = -1.60$, $\log([\mathrm{O\,II}]\ \lambda7325/[\mathrm{O\,I}]\ \lambda6300) = -0.44$, $\log([\mathrm{N\,II}]\ \lambda6583/[\mathrm{O\,I}]\ \lambda6300) = -1.18$, and $\log([\mathrm{S\,II}]\ \lambda6724/[\mathrm{O\,I}]\ \lambda6300) = -1.02$, all of which agree to within a factor of $\lesssim$2 with the observations in HN Tau at 25 AU from the star. The total flux of [O I] out the front of the shock is 0.12 ergs cm^{-2} s^{-1}, so the mean intensity is 4.4×10^{-13} ergs cm^{-2} s^{-1} arcsec^{-2}. If the average line of sight through the jet intercepts two shocks, as it would, for example, for the near and far sides of a bow shock, then the total surface brightness is close to the dereddened value of 1.3×10^{-12} ergs cm^{-2} s^{-1} arcsec^{-2}. For this model $\log N_e \sim 6.2$ in the [O I]–emitting region, by which time the ionization fraction has dropped to $\sim$0.2.

The last parameter needed to estimate a mass-loss rate is the jet velocity. The [O I] λ6300 emission extends to -160 km s^{-1} in the line profiles of HEG95; we take 250 km s^{-1} as the true velocity of the flow. The resulting mass-loss rate is then $\log \dot{M}/M_\odot\ \mathrm{yr}^{-1} = -9.3$ for the isothermal flow with $f = 0.006$. For the shock, we obtain a mass-loss rate of $\log \dot{M}/M_\odot\ \mathrm{yr}^{-1} = -8.34$, taking the preshock density of 2×10^5 cm^{-3} to fill the beam. The uncertainty in the mass-loss rate is 0.3 in log from the reddening for the two cases.

For the shock model described above, the gas cools to 6500 K after 0.05 yr and to 2000 K after 22 yr; the corresponding distances behind the shock for these two temperatures are 0.02 and 2.8 AU, respectively. These cooling distances are small compared to the width of the jet, but the cooling times are long enough that the bulk motion of the flow carries the shock a substantial distance during a cooling time. For example, a 250 km s^{-1} flow moves 53 AU (the entire projected length of the HN Tau jet) in a year.

The luminosity of [O I] λ6300, found from integrating the total counts of the [O I] image in Figure 7 and dereddening with $A_V = 1.9$, is $\log(L_{6300}/L_\odot) = -3.86$. This [O I] luminosity is a factor of 2.6 lower than that reported by HEG95. The emission equivalent width of the line is also a factor of 3.0 lower than the value of 13.2 Å observed by HEG95 (Table 2); apparently, the flux of the forbidden lines in HN Tau varies substantially. HEG95 estimated $\log \dot{M}/M_\odot\ \mathrm{yr}^{-1} = -8.1$, a factor of 1.7 higher than the current value.

3.3.6. *Flux Decline with Distance*

Because the HN Tau jet is well separated from the star, the decline of intensity with distance is insensitive to the strength of any stellar component. The intensity profile along the main jet is nearly linear in the loglinear plot in Figure 4, implying an exponential decline of the brightness with distance. A good fit to the intensity is $I \sim \exp(-r/H)$, with $H \sim 13$ AU for [O I] λ6300. By comparison, the inverse square law that appears in Figure 4 as a curved line does not fit the observations.

3.4. *Proper Motions in HH 220 and the Accretion-Outflow Connection*

HH 220 is a relatively bright emission knot $\sim$3.″5 (490 AU) from CW Tau that is visible in both the 1999 and 2000 images. The object appears round, subtends about 0.″2, and emits in [O I] λ6300, [S II] λ6724, Hα, and weakly in [O I] λ6363.

Blinking the images of HH 220 taken in 1999 and 2000 showed a clear motion away from CW Tau. The best line to measure this motion is [O I] λ6300—the red [S II] lines are blended, and the star shows velocity structure at Hα, which makes the stellar position more uncertain for that line. For the 1999.77 UT data, the separation of HH 220 from CW Tau, determined by taking one-dimensional centroids in the x- and y-directions, was $3.''50 \pm 0.''12$ at a P.A. of $152.^\circ9 \pm 0.^\circ8$. The corresponding numbers for the 2000.92 UT data are $3.''73 \pm 0.''07$ and $151.^\circ2 \pm 0.^\circ5$, respectively. The errors are dominated by uncertainties in the position of HH 220 and are 1 σ.

The radial velocity of HH 220 in [O I] 6300 is blueshifted by $\sim$120 km s^{-1} with respect to the emission at the star (Hirth et al. 1994), which introduces a shift in the position of the object along the x-direction of $\sim$0.5 pixels in the slitless data. The estimates of proper motion above include this correction, although it is less than the formal error in the x-coordinate. P.A.s of HH 220 from the two epochs fall in the middle of the range of values reported by Hirth et al. (1994), Gómez de Castro (1993), and Dougados et al. (2000). The motion of HH 220 is purely radial, within the uncertainties.

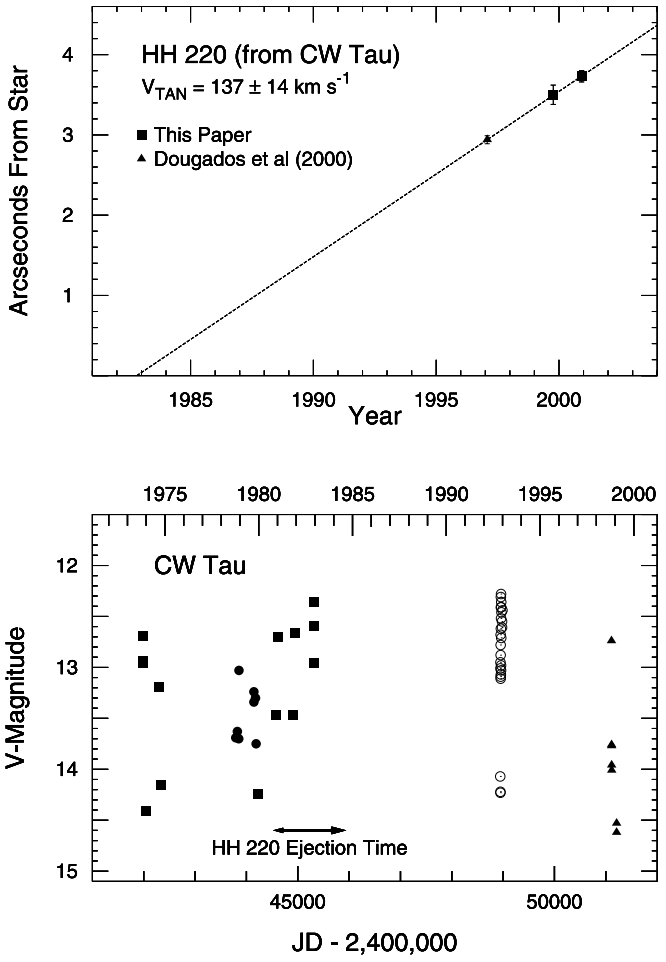

FIG. 10.—*Top*: Proper-motion measurements of HH 220. The tangential radial velocity listed assumes a distance of 140 pc to CW Tau. *Bottom*: Historical V magnitudes of CW Tau. The range of dates for the ejection of HH 220 are shown. The data prior to 1984 were found using a Web site described by Herbst et al. (1994); squares denote points from Rydgren et al. (1984), who collected values from previous sources, and filled circles are from Walker (1987). Data from Bouvier et al. (1995, *open circles*) and Oudmaijer et al. (2001, *triangles*) also appear in the plot. Although CW Tau was somewhat brighter than average during the period of ejection, the difference is not striking.

When combined with the position reported by Dougados et al. (2000) from observations taken in 1997, the two new epochs for HH 220 define the proper motion of this knot to a precision of ∼10% (Fig. 10). Assuming a distance of 140 pc, the observed proper motion of $0\farcs206 \pm 0\farcs022$ yr^{-1} translates into 137 ± 14 km s^{-1}. The observed radial velocity of ∼120 km s^{-1} implies that the jet emerges about $49^\circ \pm 10^\circ$ from the line of sight.

On the basis of these proper motions, CW Tau should have ejected HH 220 at 1982.8 ± 1.7 UT. The compilation of photometry in Figure 5 indicates that CW Tau was a bit brighter than average during that time, but the effect is small and the record is highly fragmentary. Any additional photometry from this time period would be very useful to test if HH objects originate in response to a sudden increase in the mass accretion rate, as most accretion disk models predict. Similarly, the knot at 45 AU in Figure 4 is only about 19 months old. For this reason, it is difficult to combine images taken at different epochs for highly variable objects, such as CW Tau. Fortunately, the rest of the sample is less variable, and there is typically one epoch that shows the jet well enough that the other epoch can be ignored when constructing images. In general, for studying the relationship of accretion and outflow, the best young stars for long-term photometric monitoring will be those, like CW Tau, that have strong forbidden-line emission and are highly variable.

4. SUMMARY

HST emission-line images taken with STIS in slitless mode are a powerful way to study jets as they emerge from their exciting stars. Slitless images of five classical T Tauri stars, CW Tau, DD Tau, DF Tau, HN Tau, and UZ Tau E, reveal subarcsecond jets in each system and provide information about the proper motions, collimation, and physical conditions in these jets at distances of only 10–60 AU from their driving sources. Three of the objects in our sample, DD Tau, DF Tau, and UZ Tau E, are binaries with projected separations of less than 100 AU.

We confirm that CW Tau drives a jet at P.A. $= 151^\circ$ and trace this flow in [O I] all the way to the star for the first time. The primary of the $0\farcs58$ binary DD Tau has a weak, one-sided jet with P.A. $\sim 125^\circ$. The secondary also has forbidden lines, but these are not extended. DF Tau, a classical T Tauri binary with a separation of only $\sim 0\farcs1$, shows clear jets at P.A. $= 127^\circ$ and 307°. These two jets could be a single flow or parallel flows from each star. The spectroscopic binary UZ Tau E drives a jet due north, with no evidence for a counterjet.

HN Tau is the brightest jet in our sample, is resolved spatially, and emits several lines of [O II], [Fe II], and [Ni II] not previously observed in jets close to T Tauri stars. Emission-line ratios of [O I] and [S II] show that the electron density in the jet increases near the star. We use the [Fe II] $\lambda 7155/\lambda 8617$ ratio to measure this quantity for the first time in this region, where standard density tracers, such as the red [S II] doublet ratio, are in the high-density limit. The electron density in the HN Tau jet rises from $\sim 10^6$ cm^{-3} at 30 AU to $\sim 10^7$ cm^{-3} at 5 AU.

We have constructed several diagnostic diagrams for ratios of forbidden-line emission of [O I] and [O II] over a range of densities and temperatures appropriate for stellar jets close to the star and apply these diagrams to the HN Tau jet. One can correct for the contribution of [Ca II] $\lambda 7324$ to the auroral [O II] blend (typically less than 20%) by measuring the flux of [Ca II] $\lambda 7291$. The results show that the jet has a substantial ionization fraction at distances of 5–35 AU from the star—50% for an isothermal case and 20% for gas cooling behind a shock. The large ionization fraction implies that the preshock gas must be mostly ionized, and we find good agreement with the observed fluxes and all the major forbidden-line ratios for a 40 km s^{-1} shock that moves into a mostly ionized medium with a preshock density of 2×10^5 cm^{-3}. The shock model implies a mass-loss rate of 4.6×10^{-9} $M_\odot$ yr^{-1}. In the isothermal case, the mass-loss rate is about an order of magnitude lower, and the jet has a small filling factor of ∼0.6%. The mass-loss rate varies substantially; HN Tau was observed in a relatively low state with *HST*. The brightness of the jet drops exponentially away from the star, with a scale height of 13 AU. The P.A. of the jet is 171°.

Spatial centroids of the stellar spectra are highly sensitive to any emission in a one-sided jet, although this technique only shows that the line emits in the jet and does not generate an image. All of the bright forbidden lines extend to some degree along the jet. Images and centroid plots suggest that

He I λ5876, He I λ6678, and O I λ8446 have weak jet components, although these detections are near the limit of what is possible with this technique.

Jets in HN Tau and UZ Tau E both expand with distance from the star, and the slitless images reported here are an excellent way to study jet widths. When extrapolated to the origin, the source region of UZ Tau E is unresolved, but the HN Tau jet is resolved at the 3 σ level, with a width of 5.5 ± 1.4 AU at the disk plane. The source region could be smaller than this if the jet is less collimated close to the star than it is farther out. The opening angles remain constant, within the uncertainties, from 10–60 AU for these two jets.

CW Tau ejected at least two knots within the last two decades. When combined with data from Dougados et al. (2000), the new images make it possible to measure the proper motion of the brightest of these knots, HH 220, to be 137 ± 14 km s^{-1}. The jet is inclined at $49^\circ \pm 10^\circ$ to the line of sight. The proper motions imply that CW Tau ejected HH 220 in the early 1980s. The photometric record of CW Tau from that time is incomplete and does not show any marked increases in brightness.

We thank Jon Morse for his comments on a draft of this manuscript, and Andria Schwortz for her work on the preliminary data reduction. An anonymous referee provided insightful comments in a thorough review of the submitted version of this paper. This work has been supported under NASA/*HST* grant GO-08238 from STScI.

REFERENCES

Alencar, S. H. P., & Basri, G. 2000, AJ, 119, 1881
Artymowicz, P., & Lubow, S. H. 1996, ApJ, 467, L77
Bacciotti, F., & Eislöffel, J. 1999, A&A, 342, 717
Bacciotti, F., Mundt, R., Ray, T. P., Eislöffel, J., Solf, J., & Camenzind, M. 2000, ApJ, 537, L49
Bacciotti, F., Ray, T. P., Mundt, R., Eislöffel, J., & Solf, J. 2002, ApJ, 576, 222
Barton, P. A., Donald, C. J. S., Lucas, D. M., Stevens, D. A., Steane, A. M., & Stacey, D. N. 2000, Phys. Rev. A, 62, 032503
Bastien, P. 1985, ApJS, 59, 277
Bautista, M. A., & Pradhan, A. K. 1996, A&AS, 115, 551
———. 1998, ApJ, 492, 650
Bouvier, J., Covino, E., Kovo, O., Martín, E. L., Matthews, J. M., Terranegra, L., & Beck, S. C. 1995, A&A, 299, 89
Burgess, A., Chidichimo, M. C., & Tully, J. A. 1995, A&A, 300, 627
Burrows, C. J., et al. 1996, ApJ, 473, 437
Cabrit, S., Edwards, S., Strom, S. E., & Strom, K. M. 1990, ApJ, 354, 687
Cantó, J., & Rodríguez, L. 1980, ApJ, 239, 982
Casse, J., & Ferreira, J. 2000, A&A, 361, 1178
Chidichimo, M. C. 1981, J. Phys. B, 14, 4149
Close, L. M., et al. 1998, ApJ, 499, 883
Dere, K. P., Landi, E., Mason, H. E., Monsignori Fossi, B. C., & Young, P. R. 1997, A&AS, 125, 149
Devine, D., Bally, J., Reipurth, B., & Heathcote, S. 1997, AJ, 114, 2095
Dougados, C., Cabrit, S., Lavalley, C., & Ménard, F. 2000, A&A, 357, L61
Edwards, S., Cabrit, S., Strom, S. E., Heyer, I., Strom, K. M., & Anderson, E. 1987, ApJ, 321, 473
Edwards, S., Hartigan, P., Ghandour, L., & Andrulis, C. 1994, AJ, 108, 1056
Ferreira, J. 1997, A&A, 319, 340
Garcia, P. J. V., Cabrit, S., Ferreira, J., & Binette, L. 2001, A&A, 377, 609
Ghez, A. M., Emerson, J. P., Graham, J. R., Meixner, M., & Skinner, C. J. 1994, ApJ, 434, 707
Ghez, A. M., Neugebauer, G., & Matthews, K. 1993, AJ, 106, 2005
Gómez de Castro, A. I. 1993, ApJ, 412, L43
Gómez de Castro, A. I., & Fernández, M. 1996, MNRAS, 283, 55
Gullbring, E., Hartmann, L., Briceño, C., & Calvet, N. 1998, ApJ, 492, 323
Haisch, K. E., Jr., Lada, E. A., Piña, R. K., Telesco, C. M., & Lada, C. J. 2001, AJ, 121, 1512
Hartigan, P., Edwards, S., & Ghandour, L. 1995, ApJ, 452, 736 (HEG95)
Hartigan, P., & Kenyon, S. J. 2003, ApJ, 583, 334
Hartigan, P., Kenyon, S. J., Hartmann, L., Strom, S. E., Edwards, S., Welty, A. D., & Stauffer, J. 1991, ApJ, 382, 617
Hartigan, P., Morse, J. A., & Raymond, J. 1994, ApJ, 436, 125
Hartigan, P., Morse, J. A., Reipurth, B., Heathcote, S., & Bally, J. 2001, ApJ, 559, L157
Herbst, W., Herbst, D. K., Grossman, E. J., & Weinstein, D. 1994, AJ, 108, 1906
Hillenbrand, L. A., Strom, S. E., Calvet, N., Merrill, K. M., Gatley, I., Makidon, R. B., Meyer, M. R., & Skrutskie, M. 1998, AJ, 116, 1816
Hirth, G. A., Mundt, R., & Solf, J. 1994, A&A, 285, 929
———. 1997, A&AS, 126, 437
Jensen, E. L. N., Koerner, D. W., & Mathieu, R. D. 1996, AJ, 111, 2431
Königl, A., & Pudritz, R. E. 2000, in Protostars and Planets IV, ed. V. Mannings, A. P. Boss, & S. S. Russell (Tucson: Univ. Arizona Press), 759
Kwan, J., & Tademaru, E. 1995, ApJ, 454, 382
Lavalley, C., Cabrit, S., Dougados, C., Ferruit, P., & Bacon, R. 1997, A&A, 327, 671
Leinert, Ch., Zinnecker, H., Weitzel, N., Christou, J., Ridgway, S. T., Jameson, R., Haas, M., & Lenzen, R. 1993, A&A, 278, 129
Osterbrock, D. 1989, Astrophysics of Gaseous Nebulae and Active Galactic Nuclei (Mill Valley: University Science Books)
Oudmaijer, R. D., et al. 2001, A&A, 379, 564
Pradhan, A. K., & Peng, J. 1995, in The Analysis of Emission Lines, ed. R. E. Williams & M. Livio (Cambridge: Cambridge Univ. Press), 8
Prato, L., Simon, M., Mazeh, T., Zucker, S., & McLean, I. S. 2002, ApJ, 579, L99
Pyo, T.-S., Hayashi, M., Kobayashi, N., Terada, H., Goto, M., Yamashita, T., Tokunaga, A. T., & Itoh, Y. 2002, ApJ, 570, 724
Ray, T. P., Mundt, R., Dyson, J. E., Falle, S. A. E. G., & Raga, A. C. 1996, ApJ, 468, L103
Reipurth, B., & Bally, J. 2001, ARA&A, 39, 403
Richer, J. S., Shepherd, D. S., Cabrit, S., Bachiller, R., & Churchwell, E. 2000, in Protostars and Planets IV, ed. V. Mannings, A. P. Boss, & S. S. Russell (Tucson: Univ. Arizona Press), 867
Rodríguez, M. 1999, A&A, 348, 222
Rydgren, A. E., Schmelz, J. T., Zak, D. S., & Vrba, F. J. 1984, Publ. US Naval Obs., 25, pt. 1
Shang, H., Shu, F. H., & Glassgold, A. E. 1998, ApJ, 493, L91
Shu, F. H., Najita, J. R., Shang, H., & Li, Z.-Y. 2000, in Protostars and Planets IV, ed. V. Mannings, A. P. Boss, & S. S. Russell (Tucson: Univ. Arizona Press), 789
Solf, J. 1987, A&A, 184, 322
Tamazian, V. S., Docobo, J. A., White, R. J., & Woitas, J. 2002, ApJ, 578, 925
Tamura, M., & Sato, S. 1989, AJ, 98, 1368
Valenti, J. A., Basri, G., & Johns, C. M. 1993, AJ, 106, 2024
Verner, E. M., Verner, D. A., Baldwin, J. A., Ferland, G. J., & Martin, P. G. 2000, ApJ, 543, 831
Walker, M. F. 1987, PASP, 99, 392
White, R. J., & Ghez, A. M. 2001, ApJ, 556, 265
Woitas J., Ray, T. P., Bacciotti, F., Davis, C. J., & Eislöffel, J. 2002, ApJ, 580, 336
Young, P. R., Del Zanna, G., Landi, E., Dere, K. P., Mason, H. E., & Landini, M. 2003, ApJS, 144, 135